The Astrophysical Journal, 645:868–889, 2006 July 10

HIGH-RESOLUTION ABSORPTION SPECTROSCOPY OF MULTIPHASE, HIGH-METALLICITY GAS ASSOCIATED WITH THE LUMINOUS QUASAR HE 0226−4110[1]

Rajib Ganguly,[2,3] Kenneth R. Sembach,[2] Todd M. Tripp,[4] Blair D. Savage,[5] and Bart P. Wakker[5]

Received 2005 November 11; accepted 2006 March 15

ABSTRACT

We present *FUSE* and *HST* STIS observations of the absorption-line system near the emission redshift of the radio-quiet, X-ray-bright quasar HE 0226−4110 ($z = 0.495$, $V = 15.2$). The spectra cover the rest-frame wavelength range 610–1150 Å, and we detect a wide range of ionization species, including four adjacent stages of oxygen: O III–VI, which reveal a striking change in gas kinematics with ionization. Examinaton of the O VI $\lambda\lambda$1031, 1037 doublet profiles reveals no evidence for partial coverage or unresolved saturated structure. O III is only detected in a narrow feature that is also traced by the H I and C III lines, suggesting that they arise in the same gas. Absorption at the same velocity is also present in other species (N IV, O IV–VI, S IV, and possibly Ne VIII), but the kinematics differ from the O III, implying production in separate gaseous phases. The combination of H I, O III , and C III information yields an estimate of both the photoionization parameter and the metallicity of the O III–bearing gas: $[\mathrm{O/H}] = +0.12^{+0.16}_{-0.03}$, $\log U = -2.29^{+0.02}_{-0.23}$. We discuss two possible locations for the gas in this associated absorption-line system: the narrow emission line region of the quasar, and the halo of the quasar host galaxy. An additional narrow (and thus photoionized) component that is only detected in O VI appears 58 km s^{-1} redward of the O III–bearing gas with $-0.35 \lesssim \log U \lesssim 0.02$. Additional structure is detected in the associated absorber in the form of two broad components that only appear in moderate- to high-ionization species.

Subject headings: quasars: absorption lines — quasars: emission lines — quasars: individual (HE 0226−4110) — ultraviolet: ISM

Online material: color figures

1. INTRODUCTION

Early after the discovery of quasars, it was recognized that their extreme luminosities, nonthermal spectra, variability, and compact sizes were readily achieved through the release of gravitational energy of matter accreting onto supermassive black holes (e.g., Greenstein & Schmidt 1964; Schmidt 1963). The remarkable result from the previous decade of work that nearly all galaxies host central supermassive black holes (e.g., Tremaine et al. 2002; Gebhardt et al. 2000; Ferrarese & Merritt 2000; Magorrian et al. 1998) seems to suggest that any galaxy has the potential to host a quasar (or other form of active nucleus). In tandem with the observed fact that the quasar luminosity function peaks at $z \sim 2$ (e.g., Boyle et al. 2000) and falls off thereafter suggests that the quasar phenomenon is possibly a phase of galaxy evolution. Consequently, in order to trace the history of gas in the universe, it is important to understand how accretion disks around supermassive black holes are fueled, the dynamics and geometry of the accreting/outflowing gas, and how some fraction of the gas is returned to the intergalactic medium (IGM; i.e., feedback). A complete description of how gas falls into galaxies and is subsequently processed should include an understanding of the physical origin of absorption-line systems that appear to cluster around quasars (hereafter "associated" absorption lines, or AALs;[6] e.g., Weymann et al. 1979; Foltz et al. 1986, 1988). Are there dynamical/kinematic relationships between the gas and those regions? Where is the gas located? What are the physical properties of the gas? Are AALs just weather around quasars or do they probe physically interesting regions around the black hole like the broad/narrow emission line region? Are AALs an integral feature of the quasar phenomenon?

The current paradigm of quasars holds that the disk of matter accreting onto the central supermassive black hole that powers quasars is also the origin of a wind (e.g., Elvis 2000; Proga et al. 2000; Murray et al. 1995). This wind is thought to result from gas that is lifted off the accretion disk via local radiation pressure and then radially driven away from the black hole via scattering of ultraviolet lines. This scenario has been quite successful at explaining the existence and shape of both broad absorption lines (BALs) and the high-ionization broad emission lines. Low-ionization and high-excitation lines are more complicated as these may have a contribution from the outer regions of the accretion-disk itself (e.g., Eracleous & Halpern 2004). There are indications, including temporal variability of profiles and partial occultation of the absorber over the background quasar, that some fraction of narrow absorption-line systems also probe this outflowing gas (e.g., Ganguly et al. 2003; Misawa et al. 2003; Yuan et al. 2002).

[1] Based on observations made with the NASA/ESA *Hubble Space Telescope*, which is operated by the Association of Universities for Research in Astronomy, Inc., under NASA contract NAS 5-26555. Also based on observations made with the NASA-CNES-CSA Far Ultraviolet Spectroscopic Explorer, which is operated for NASA by Johns Hopkins University under NASA contract NAS 5-32985.

[2] Space Telescope Science Institute, 3700 San Martin Drive, Baltimore, MD 21218.

[3] Department of Physics and Astronomy, University of Wyoming (Department 3905), 1000 East University Avenue, Laramie, WY 82071.

[4] Department of Astronomy, University of Massachusetts, Amherst, MA 01003.

[5] Department of Astronomy, University of Wisconsin-Madison, 475 North Charter Street, Madison, WI 53706.

[6] Following Foltz et al. (1986), we refer to any narrow absorption line that arises within 5000 km s^{-1} as an AAL. We distinguish this purely observational classification from absorption that is truly related (i.e., intrinsic) to the quasar central engine or host galaxy.

In sight lines to high-redshift QSOs ($z \sim 2.5$) that are selected based on radio brightness, as many as 30% of C IV–selected systems with $z_{abs} \ll z_{em}$, commonly assumed to arise from the halos of intervening galaxies, may be intrinsic to the QSO (Richards et al. 1999, 2001). This frequency was estimated by examining differences in the distribution of C IV–selected systems in apparent ejection velocity (over the range $+75,000 \geq v_{ej} \geq -6000$ km s^{-1}) as a function of quasar radio loudness and spectral index. If C IV–selected systems are unrelated to the background quasar (as in the case of halos from cosmologically distributed interloping galaxies), then no variation is expected. In the apparent ejection velocity range +6000 to +75,000 km s^{-1} (i.e., at large separations from the quasar redshift), Richards (2001) found a statistical excess of C IV systems toward radio-quiet quasars compared to radio-loud quasars, and in flat-spectrum quasars compared to steep-spectrum quasars.

This estimate of the frequency of high-ejection velocity systems is surprisingly high given that, at lower redshifts, many studies have shown that absorption systems with $z_{abs} \ll z_{em}$ are strongly correlated with foreground galaxies, indicating that these low-z absorbers are *not* intrinsic systems with high ejection velocities. It is not yet clear how these observations can be reconciled. Studies to understand the populations of absorbing galaxies at high redshift (i.e., $z_{abs} \gtrsim 1.5$) are not yet feasible with current technology. Likewise, it is possible that the selection of optically bright low-redshift quasars in follow-up studies of absorbing galaxy populations has an effect on the velocity distribution of intrinsic systems such that they are not observed.

In a heterogeneous study of low-redshift quasars, Wise et al. (2004) have found that at least 20% of low-z AALs (i.e., systems appearing within 5000 km s^{-1} of the quasar redshift) show time variability and therefore are likely to be intrinsic. While intrinsic absorbers that lie at large velocity separations from the quasar likely originate in some form of high-velocity outflow, there are additional possible locations for AALs: ablation off an obscuring torus (Krolik & Kriss 2001), the narrow emission line region, the quasar host galaxy (e.g., Baker et al. 2002), satellite dwarfs, or luminous companion galaxies in the quasar's host cluster.

There has been considerable statistical work on the relationship between associated absorbers and various quasar properties. Foltz et al. (1986, 1988) established that intermediate-redshift AALs ($1.43 \lesssim z \lesssim 1.94$) with large C IV equivalent widths [W_{rest}(C IV) $\gtrsim 1.5$ Å] preferentially appear toward steep-spectrum radio-loud quasars, in stark contrast with BALs, which prefer more radio-quiet quasars (e.g., Becker et al. 2000). While the dichotomy in radio-loudness in quasars has apparently been eliminated through deep radio imaging by the FIRST (Faint Images of the Radio Sky at Twenty cm) survey (Becker et al. 1995), there remains an unexplained discrepancy between quasar radio-loudness and the presence of intrinsic absorption. Ganguly et al. (2001a) reported an apparent dearth of strong AALs among the lower redshift ($z < 1$) quasars observed with the *Hubble Space Telescope* (*HST*) for the *HST* Quasar Absorption Line Key Project, suggesting possible evolution in the frequency of strong AALs. While the absence of strong AALs in that sample might be explained partially as a bias against bluer quasars, there is still evidence for evolution from larger and well-selected quasar samples (Brandt et al. 2000; Vestergaard 2003).

As noted by several authors (e.g., Mathur et al. 1995; Brandt et al. 2000), there is apparently a connection between C IV–selected AALs, and absorption at soft X-ray wavelengths (so-called warm absorbers). The precise nature of this connection is perplexing given the drastically different ionization potentials of species (e.g., O VII, O VIII) that exist in warm absorbers. A number of campaigns have been carried out employing simultaneous *HST* Space Telescope Imaging Spectrograph (*HST* STIS), *Far Ultraviolet Spectroscopic Explorer* (*FUSE*), and *Chandra X-Ray Observatory*/*XMM-Newton* spectroscopy of Seyfert galaxies, the lower luminosity kin of quasars, such as NGC 3783 (Netzer et al. 2003; Gabel et al. 2003a, 2003b; Kaspi et al. 2002), Mrk 279 (Scott et al. 2004b) and NGC 5548 (Crenshaw et al. 2003). The results of these studies of Seyfert galaxies in regards to the general relationship between the X-ray and UV absorbing gas is inconclusive. In some cases, the absorbers can be explained by the same phase of gas; in other cases, a more complex, multiphase absorber is required. For the more luminous quasar 3C 351, Yuan et al. (2002) have analyzed high-resolution UV and X-ray spectra and find that complex, multiphase gas is required to explain the components in the AAL.

Like the previously mentioned campaigns, it is important to temper statistical relationships between absorbers and quasar properties with case studies of individual objects. Since the demographics of the absorbers are clearly eclectic, only case-by-case classifications to identify subsamples can hope to recover true, undiluted physical relationships. Using *HST* STIS and *FUSE* observations of low-redshift quasars that cover the O VI $\lambda\lambda$1031.927, 1037.617 doublet, not only can we bridge the gap between C IV–selected AALs and soft X-ray "warm absorbers," but we can also take advantage of the high spectral resolution to understand the physical properties and origin of the gas. Kriss (2002) presents a summary of *FUSE* observations of bright active galactic nuclei (AGNs) at low redshift (predominantly Seyfert galaxies). These observations survey the O VI doublet in AGNs out to $z \sim 0.15$. In a companion paper, we extend this survey out to $z \sim 0.5$ (R. Ganguly et al. 2006, in preparation).

In this paper we report the discovery of a remarkable absorption-line system ($z_{abs} = 0.4925$) near the redshift of the radio-quiet, X-ray-bright quasar HE 0226−4110 ($z_{em} = 0.495, V = 15.2$; Reimers et al. 1996). In § 2 we discuss the details of our *HST* STIS and *FUSE* observations. In § 3 we investigate the properties of the quasar to provide a context for understanding the associated absorption presented and analyzed in § 4. Finally, in § 5 we summarize our results and discuss the implications of our findings.

2. DATA

2.1. *STIS Observations*

Our *HST* STIS (Woodgate et al. 1998; Kimble et al. 1998) observations were carried out using the $0\farcs2 \times 0\farcs06$ slit, the E140M grating, and the near-UV MAMA detector between 2002 December 25 and 2003 January 1. The total integration time of the observations was 43.8 ks. This configuration provides a spectral resolution of about 6.5 km s^{-1} (FWHM) with a sampling of 2–3 pixels per resolution element, and yields semicontinuous spectra over the observed wavelength range 1149–1729.5 Å. The data were reduced and calibrated as described by Tripp et al. (2001). For further details on the processing of the data sets used in this work for the HE 0226−4110 sight line, see Fox et al. (2005) and Savage et al. (2005). According to Quijano et al. (2003), the zero-point heliocentric velocity uncertainty in the calibration is about 0.2–0.5 pixels, or ~0.6–1.5 km s^{-1}. The flux calibrations are good to 8% [or roughly $(1-2) \times 10^{-15}$ ergs cm^{-2} s^{-1} Å^{-1} for these data]. The integrations yielded a final signal-to-noise per resolution element (after reduction, calibration, and co-addition of spectra) of ~11 at 1300 Å and ~8.5 at 1500 Å.

Selected portions of the STIS echelle spectrum of HE 0226−4110 are shown in Figure 1. The top panel of Figure 1 shows a

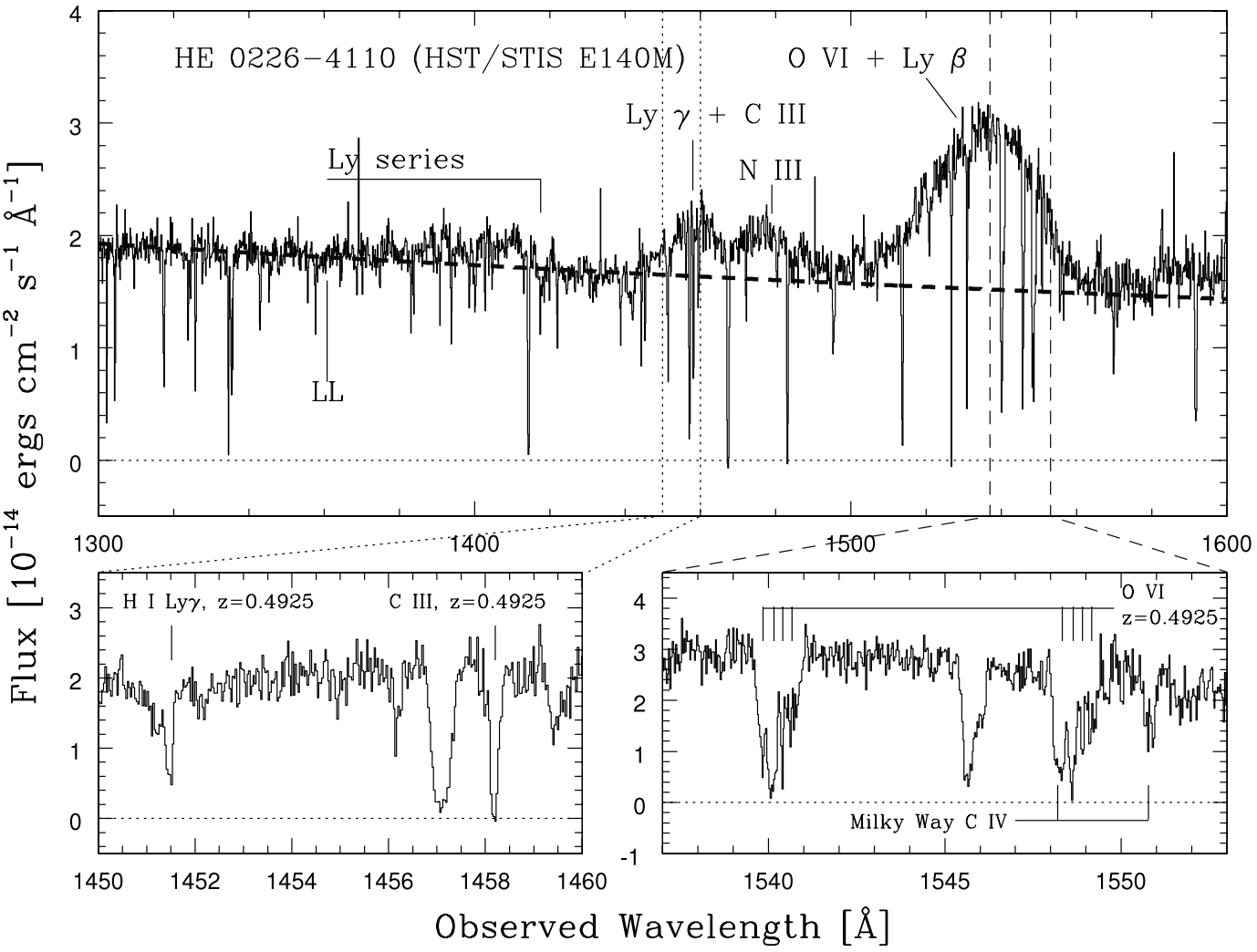

FIG. 1.—Portions of the STIS E140M echelle spectrum of HE 0226−4110. In order to improve the signal-to-noise ratio and thereby show the continuum and emission-line shapes more clearly, the top panel is binned to a sampling of ~20 km s^{-1}. In the top panel, the thick dashed line shows the power law fitted to the continuum for the purposes of the photoionization models presented in the text (see §§ 3.1 and 4.1). The O VI + Lyβ, N III, Lyγ + C III, and higher order Lyman series emission lines of the QSO are marked. An "LL" marks the location of the Lyman limit for the associated absorption-line system. The bottom panels show selected associated absorption lines at $z_{abs} = 0.4925$ including, H I Lyγ and C III λ977.020 (*bottom left panel*) and the O VI $\lambda\lambda$1031.926, 1037.617 doublet (*bottom right panel*). The bottom panels are binned to ~7 km s^{-1} pixels. Note that the O VI λ1037.617 line is blended with one of the lines of the Galactic C IV $\lambda\lambda$1548.204, 1550.781 doublet, which is also marked. [*See the electronic edition of the Journal for a color version of this figure*.]

broad section of the spectrum including the O VI + Lyβ broad emission line of the QSO, as well as several weaker emission features. We also show in the upper panel a power law fitted to the QSO continuum (see § 3.1), which we use for photoionization modeling in § 4.1. The spectrum is rich in Galactic and extragalactic absorption lines. Extragalactic intervening absorption systems (i.e., with $z_{abs} \ll z_{em}$) in the spectrum of HE 0226−4110 are analyzed and discussed in Savage et al. (2005) and Lehner et al. (2006), and Galactic absorption lines and high-velocity clouds toward this QSO are discussed by Collins et al. (2005) and Fox et al. (2005).

Examples of the associated absorption lines of interest in this paper that are redshifted into the STIS-E140M band are shown in the bottom panels of Figure 1, including the multicomponent O VI $\lambda\lambda$1031.926, 1037.617 doublet at $z_{abs} = 0.4925$ (*bottom right panel*) and the H I Lyγ and C III λ977.020 lines (*bottom left panel*). It is immediately evident that this is a complex, multiphase absorber: four components are present in the O VI lines, spread over a velocity range of 250 km s^{-1}, but only a single component is seen in tracers of lower ionization gas such as C III and Lyγ (the weak component blueward of the Lyγ line shown in Fig. 1 is an unrelated Lyα line at a different redshift). We also see from this figure that the associated O VI λ1037.617 line at $z_{abs} = 0.4925$ is blended with Milky Way C IV λ1548.204. This blend is not a serious problem because the O VI λ1031.926 line is free of blending, and the Galactic C IV λ1550.781 transition is also unblended, which enables an assessment of the degree of contamination from C IV λ1548.204.

2.2. *FUSE Observations*

Our *FUSE* observations were carried out using the LWRS aperture between 2000 December 12 and 2003 October 21 for a total integration time of 208.9 ks. In this mode, the *FUSE* satellite delivers spectra with velocity resolution in the range 20–30 km s^{-1}, with 10 pixels per resolution element. For further details about *FUSE* and its on-orbit performance, see Moos et al. (2000) and Sahnow et al. (2000). The data were reduced using version 2.4.0 of the CALFUSE pipeline; see Fox et al. (2005) and Savage et al. (2005) for further details regarding subsequent wavelength calibration steps and combination of subintegrations. (We note that

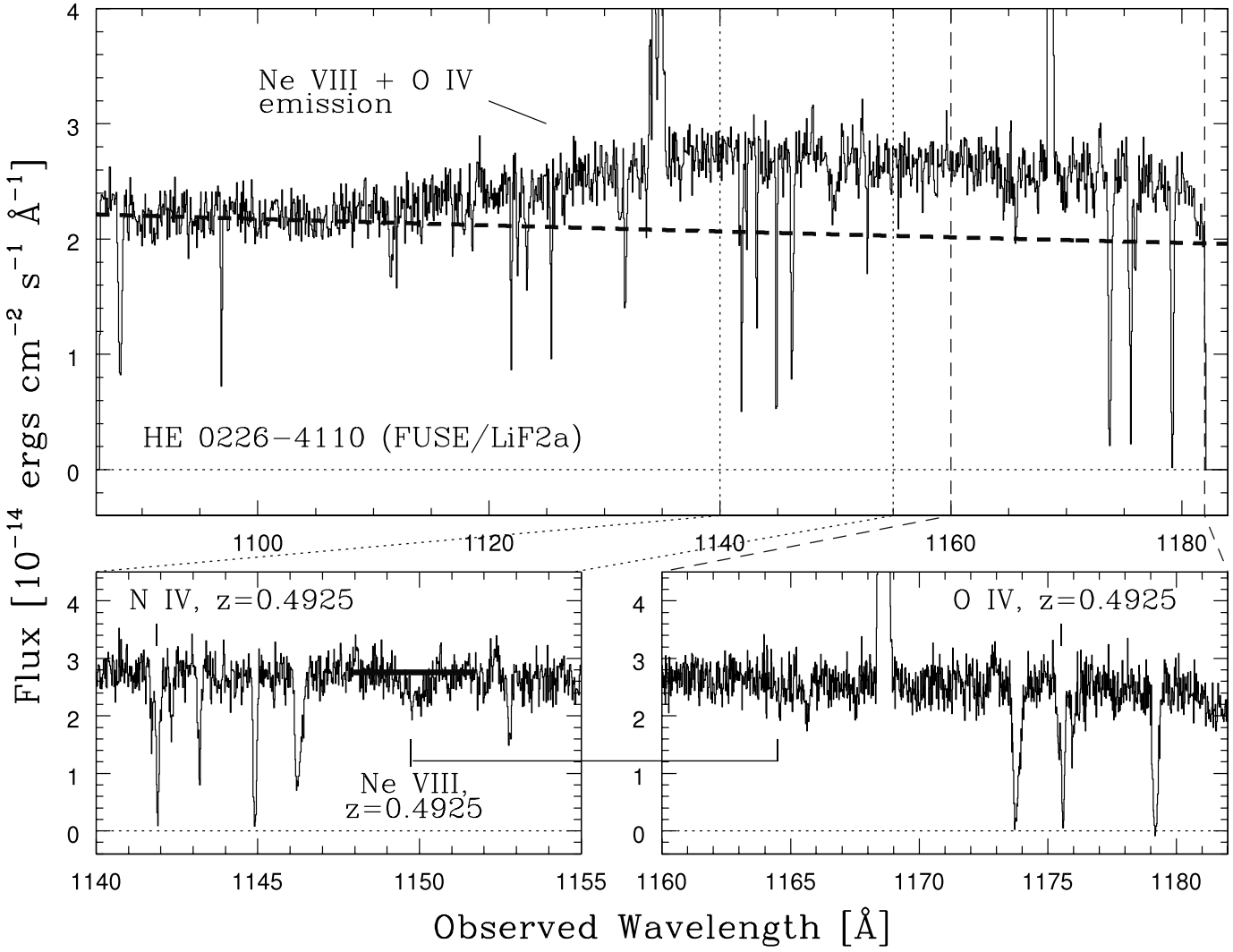

FIG. 2.—Portions of the *FUSE* LiF2A spectrum of HE 0226−4110. In order to improve the signal-to-noise ratio and thereby show the continuum and emission-line shapes more clearly, the top panel is binned to a sampling of ~20 km s^{-1}. In the top panel, the thick dashed line shows the power law fitted to the continuum for the purposes of the photoionization models presented in the text (see §§ 3.1 and 4.1), and the Ne VIII + O IV emission line of the QSO is marked. The bottom panels show selected associated absorption lines at $z_{abs} = 0.4925$ including N IV λ765.148 (*bottom left*), O IV λ787.711 (*bottom right*), and the Ne VIII $\lambda\lambda$770.409, 780.324 doublet (*both bottom panels*). In the bottom left panel, our local Legendre-polynomial fit to the continuum around the Ne VIII λ770.409 line is shown as a thick line. The Ne VIII λ780.324, which would nominally appear in the bottom right panel, is not detected. The bottom panels are binned to a sampling of ~6 km s^{-1}. [*See the electronic edition of the Journal for a color version of this figure.*].

over the 34 month span of the observations, the quasar continuum level increased by about 25%.) In this study, we use primarily the LiF2A and SiC2A detector segments that cover the wavelength ranges 1086.3–1182.0 and 916.5–1006 Å, respectively. In addition, the *FUSE* data are rebinned to a sampling of about 3–4 bins per resolution element. The CALFUSE pipeline and subsequent processing provides fully calibrated (flux and wavelength) spectra that are accurate to 5 km s^{-1} in wavelength and about 10% [(1–2) × 10^{-15} ergs cm^{-2} s^{-1} Å^{-1}] in flux. [Note that the *FUSE* spectra were aligned with the STIS spectra using Galactic and intervening absorption lines; see § 2.3.] The long integration time on this bright quasar provided a signal-to-noise ratio of 23 per resolution element at 1150 Å (in the LiF2A detector segment) and 13 per resolution element at 950 Å (in the SiC2A detector segment).

Selected portions of the *FUSE* LiF2A spectrum are shown in Figure 2. The top panel of the figure shows the entire portion of the *FUSE* spectrum that is covered by the LiF2A detector segment. For clarity, the spectra in this panel are shown with a sampling of ~20 km s^{-1}, or 1 bin per *FUSE* resolution element in this region of the spectrum. The underlying QSO continuum from the power-law fit to the STIS spectrum is also shown; the contribution of the Ne VIII and O IV broad emission lines is readily apparent.

In the bottom panels, we show examples of the associated absorption lines that are clearly detected in this spectrum. In these panels, the spectra are shown with a sampling of ~6 km s^{-1}. The lower left panel shows the portion of the spectrum covering the associated absorption from the N IV λ765.148 and Ne VIII λ770.409 lines. In this panel we also overlay our Legendre-polynomial fit to the local continuum around the Ne VIII λ770.409 line to show that the detection of the feature is robust. The line, which appears at an observed wavelength of ~1150 Å, is also readily apparent in the top panel. In the bottom right panel, we show another region of the *FUSE* LiF2A spectrum that covers the Ne VIII λ780.324 and O IV λ787.711 lines. The Ne VIII λ780.324 line is not detected in our spectrum down to a 3 σ equivalent width limit of 103 mÅ. The Ne VIII λ770.409 line has an equivalent width of 140 ± 22 mÅ, so the nondetection of the weaker line is consistent with

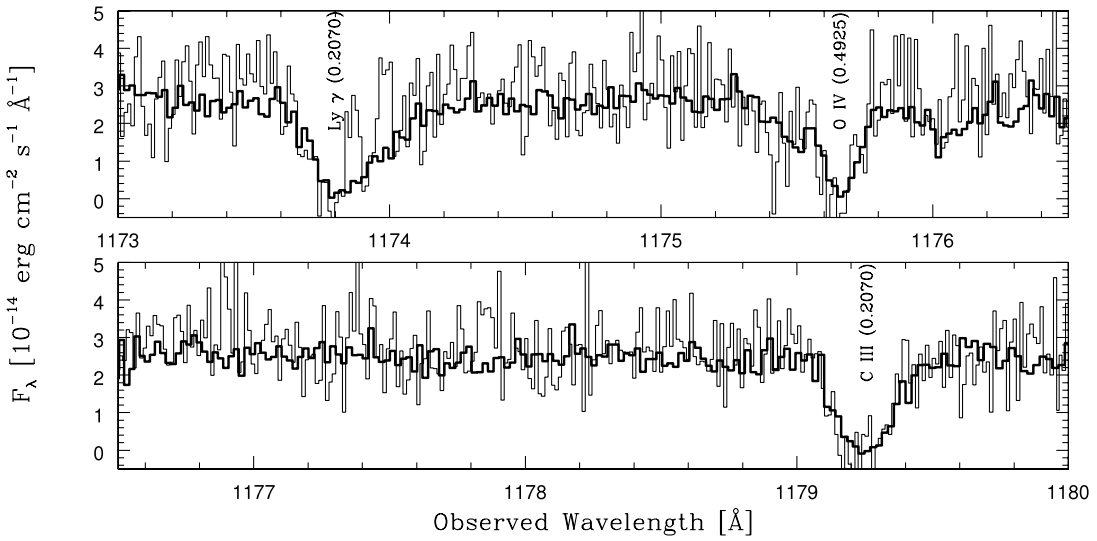

FIG. 3.—Portion of the overlapping region between the *FUSE* LiF2A (*thick histogram*) and STIS E140M (*thin histogram*) spectra. The plotted region contains associated absorption from O IV, as well as IGM absorption from Lyγ and C III. [*See the electronic edition of the Journal for a color version of this figure.*]

a physically meaningful doublet ratio [i.e., $1 \leq W_\lambda(\lambda770.409)/W_\lambda(\lambda780.324) \leq 2$]. We conclude that the detection of the absorption feature at $\sim$1150 Å and its identification with the Ne VIII λ770.409 line is reliable.

2.3. *A Remark on the Wavelength Cross-Calibration*

Of particular importance to this study, the *FUSE* and STIS data were aligned to a common (heliocentric) wavelength scale using the Galactic C II $\lambda\lambda$1334.532, 1036.337 and Fe II $\lambda\lambda$1144.938, 1608.451 lines, as well as the Lyγ and C III λ977.020 IGM lines of the $z_{\rm abs} = 0.2070$ absorber. The latter two lines appear in the wavelength region 1149–1182 Å, where the *FUSE* and STIS spectra overlap. A portion of the overlapping region is shown in Figure 3. The shift required to align the *FUSE* spectra to the heliocentric velocity scale provided by the STIS calibration was 3–5 km s^{-1}, which is within the residual zero-point uncertainty reported by Fox et al. (2005). The alignment of these spectra is important to this study, because there is an apparent ionization-dependent velocity shift in the AAL at $z_{\rm abs} = 0.4925$ between the O III λ832.927 line and the O IV λ787.711 line (see § 4.1). The former line appears in the STIS spectra, while the latter line appears in the overlapping region and is flanked by two IGM lines from the same system (at $z_{\rm abs} = 0.2070$). The alignment of the IGM features gives us confidence in the magnitude of the shift, and, consequently, in the reality of the apparent velocity shift in the associated absorber.

2.4. *Comments on* Ne VIII

The detection of the high-ionization Ne VIII λ770.409 line is fortuitous as it provides a further bridge between lower ionization associated C IV absorption and the higher ionization X-ray absorption by O VII and O VIII (e.g., Mathur et al. 1995; Brandt et al. 2000). To our knowledge, Ne VIII has only been detected in associated narrow absorption in three other quasars, UM 675 (Hamann et al. 1995), 3C 288.1 (Hamann et al. 2000), HDFS-QSO J2233−606 (Petitjean & Srianand 1999), and possibly HS 1700+6416 (Petitjean et al. 1996). Previous detections of Ne VIII absorption in BAL QSOs include PG 0946+301 (Arav et al. 1999), SBS 1542+541 (Telfer et al. 1998), and Q0226-1024 (Korista et al. 1992). We note also that the *FUSE composite* spectrum of Scott et al. (2004a) shows a peculiar absorption feature just blueward of the Ne VIII + O IV emission at a rest wavelength of $\sim$730 Å. (As noted by Scott et al. [2004a], this feature was also present, although at a much weaker level, in the rest-frame extreme ultraviolet *HST* composite from Telfer et al. [2002].) The HE 0226−4110 *FUSE* spectrum presented here was used in that composite, but the associated absorber does not contribute to that feature.

3. QUASAR PROPERTIES

Before proceeding with an analysis of the associated absorption at $z_{\rm abs} = 0.4925$, we first discuss the general UV/optical, radio, and X-ray properties of the quasar, as this is important to understanding the environment of the absorbing gas.

3.1. *UV/Optical*

The redshift of the quasar as measured by the peak of the Mg II emission line (Reimers et al. 1996) is $z_{\rm em} = 0.495 \pm 0.001$. In general, it is more favorable in the study of associated absorbers to use redshifts determined from narrow emission lines (as these can be measured to higher precision) or from high-excitation lines, which are thought to arise from the quasar accretion disk (not the outflow), and may more accurately reflect the systemic redshift. To this end, we have analyzed the optical spectrum obtained by Grupe et al. (1999) using the ESO Faint Object Spectrograph and Camera ($\approx$5 Å FWHM resolution with 1.2 Å pixel^{-1} sampling). The spectrum covers the Hβ and [O III] λ5007 emission lines and is shown in Figure 4. (At the redshifted position of the [O III] λ5007 line, the resolution of the spectrum is $\approx$200 km s^{-1} with a sampling of 48 km s^{-1}.) Since the Hβ and [O III] λ5007 emission lines lie on top of an Fe II multiplet, we model the spectrum with an underlying power-law continuum with Gaussian emission-line components:

$$F_\lambda = F_{\lambda_0}\left[\left(\frac{\lambda}{\lambda_0}\right)^{\beta} + \sum_{i=1}^{m} w_i e^{-1/2(\lambda-\lambda_i/\sigma_i)^2}\right], \qquad (1)$$

where λ_0 is an arbitrary reference wavelength, F_{λ_0} is the normalizing continuum flux at that wavelength, β is the continuum power-law index, m is the number of emission-line components, and w_i, λ_i, and σ_i are the relative strength, central wavelength, and

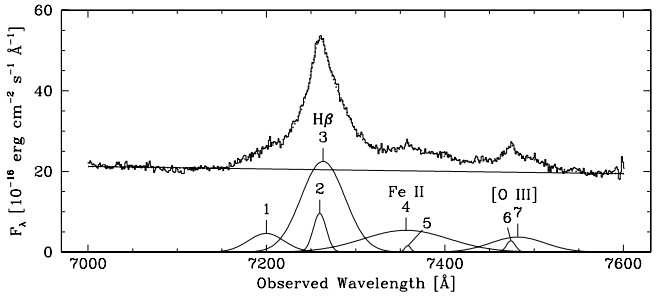

FIG. 4.—Portion of the Grupe et al. (1999) optical spectrum of HE 0226−4110 (*histogram*) that covers the Hβ and [O III] λ5007 lines. The smooth curves show the contributions to the best fit from the underlying power-law continuum and each emission-line component. The dotted curve shows the total best-fit spectrum. Each emission-line component is coded with a number that appears over the component that is used to cross-reference with the fit parameters listed in Table 1. The locations of the Hβ, Fe II, and [O III] emission lines are also labeled. [*See the electronic edition of the Journal for a color version of this figure*.]

width of each emission-line component, respectively. We used a Marquardt-Levenburg least-squares algorithm (Press et al. 1992) to determine the best-fit for a given number of emission components, and the *F*-test to choose the optimal number of statistically significant components. In our fitting algorithm, we use the entire spectrum and allow both power-law and emission-line parameters to vary simultaneously to minimize the χ^2 (defined in the usual manner). The errors on all parameters are given by the diagonal elements of the covariance matrix (the inverse of the χ^2 curvature matrix). In Figure 4 we also show the best-fit model, as well as the separate contributions from the power-law continuum and each emission-line component. The parameters of the fit are listed in Table 1. The fit appears reasonable, especially in regions far from the emission lines, so we are confident in the parameters of the underlying power law.

Both the Hβ and [O III] λ5007 emission lines are well described by the superposition of a broad component (FWHM = 2861 ± 191 km s^{-1}) at $z_{\rm em} = 0.4938 \pm 0.0001$ and a narrow component (FWHM = 966 ± 86 km s^{-1}) at $z_{\rm em} = 0.4928 \pm 0.0001$. Three additional components are required to yield a good fit to the data. We identify one component with the Fe II λ4924 multiplet. Since our goal is only to measure the redshift and intensity of the [O III] λ5007 line (to compare with the associated absorption in the O III λ832.927 line), we do not attempt to further model the Fe II emission.

In addition to the fit of the optical continuum and emission lines, we have also fit the STIS spectrum that includes the Lyman limit of the associated absorber. This is important for characterizing the ionizing radiation field assumed later in our photoionization models. Our method for fitting the UV spectrum was identical to that of the optical spectrum (described above), and the underlying power law is shown in Figure 1. The extrapolation of this power law to the *FUSE* band is also shown in Figure 2. In both figures, the fit appears quite reasonable. The parameters of the power-law fit are $F_{\lambda_0} = (1.74 \pm 0.01) \times 10^{-14}$ ergs cm^{-2} s^{-1} Å^{-1}, $\beta = -1.42 \pm 0.02$ at $\lambda_0 = 1395.55$ Å. We recast this fit into frequency units ($F_\nu \propto \nu^{\alpha_{\rm UV}}$) and to the rest frame of the quasar: $F_{\nu_0} = (5.00 \pm 0.03) \times 10^{-27}$ ergs cm^{-2} s^{-1} Hz^{-1}, $\alpha_{\rm UV} = -0.58 \pm 0.02$ at 1 ryd. As in Table 1, we adopt a luminosity distance of 2774.9 Mpc ($z = 0.493$ for a $\Omega_\Lambda = 0.73$, $\Omega_m = 0.27$ cosmology). Thus, the luminosity density of the quasar at 1 ryd is $\log L_\nu[\text{ergs s}^{-1}\ \text{Hz}^{-1}] = 30.65$.

3.2. *Radio*

Another important quasar property to consider in understanding this associated absorber is the radio-loudness (defined as the ratio of flux densities at 5 GHz and 2500 Å, R^*), since it appears that absorption that is clearly related to quasar outflows (i.e., broad absorption lines) is connected to the presence and strength of radio emission. The precise nature of this connection is not yet clear. Strong, narrow, associated C IV absorption is preferentially found in steep-spectrum, radio-loud ($R^* > 10$) quasars (e.g., Foltz et al. 1988; Vestergaard 2003), while broad absorption lines are predominantly found in radio-quiet quasars (e.g., Turnshek 1988; Weymann et al. 1991; Brotherton et al. 1998; Becker et al. 2000).

This quasar is not detected by the Parkes-MIT-NRAO survey (Griffith & Wright 1993) down to a 4.4 σ flux density limit of 47.3 mJy at 4.85 GHz. This limit corresponds to a radio-loudness of $\log R^* < 1$, which is radio-quiet by the definition of Kellermann et al. (1989). The radio-loudness is an apparently important indicator of the soft X-ray spectral slope (Laor et al. 1997), as well as being one of a collection of properties (including the [O III] λ5007 luminosity, and Hβ emission-line FWHM intensity) that are apparently related among optically selected quasars (that is, Eigenvector 1 from the principal components analysis of Boroson

TABLE 1
PARAMETERS OF FIT TO OPTICAL SPECTRUM

Component	w_i[a]	λ_i (Å)	FWHM$_i$[b] (km s^{-1})	Identification	$z_{\rm em}$	$\log \lambda L_\lambda$[c] (erg s^{-1})
1	0.22 ± 0.02	7199.6 ± 2.9	1968 ± 178	Unidentified	...	43.33 ± 0.05
2	0.45 ± 0.07	7259.7 ± 1.0	710 ± 124	Hβ	0.4929 ± 0.0001	43.21 ± 0.10
3	1.06 ± 0.06	7263.4 ± 1.0	2376 ± 117	Hβ	0.4937 ± 0.0001	44.10 ± 0.03
4	0.25 ± 0.01	7356.5 ± 3.1	4610 ± 414	Fe II	...	43.78 ± 0.04
5	0.07 ± 0.02	7358.4 ± 0.8	319 ± 85	Unidentified[d]	...	42.09 ± 0.16
6	0.13 ± 0.02	7474.0 ± 0.8	466 ± 86	[O III] λ5007	0.4928 ± 0.0001	42.51 ± 0.11
7	0.18 ± 0.01	7481.6 ± 2.0	2861 ± 191	[O III] λ5007	0.4942 ± 0.0002	43.42 ± 0.04

NOTES.—Uncertainties are quoted at 1 σ confidence. The best-fit flux normalization at 7000 Å is $F_{\lambda_0} = (2.125 \pm 0.05) \times 10^{-15}$ ergs cm^{-2} s^{-1} Å^{-1}. The best-fit power-law index was $\beta = -1.07 \pm 0.09$ ($F_\lambda \propto \lambda^\beta$). See § 3 for explanations of the parameters.

[a] Emission-line strengths are quoted relative to best-fit flux normalization at 7000 Å.

[b] The width of the emission-line components is quoted as the FWHM intensity (2.35 σ_i).

[c] The line luminosity for each component was computed assuming isotropic radiation and a luminosity distance of 2774.9 Mpc ($z = 0.493$ for a $\Omega_\Lambda = 0.73$, $\Omega_m = 0.27$ cosmology).

[d] One possible identification of this emission-line component is [O III] λ4959. However, this is not consistent with either the centroids or strengths of the listed [O III] λ5007 components. There are potential systematic effects resulting from an improper accounting of the underlying Fe II emission, but such an accounting is beyond the scope of this work.

& Green 1992). The underlying connection among these properties is generally interpreted as the accretion-rate of material onto the black hole relative to Eddington, $\dot{M}/\dot{M}_{\rm edd}$. The radio-loudness of this quasar and its relatively weak [O III] λ5007 emission indicate that the accretion-rate relative to Eddington is low in comparison with other quasars.

3.3. *Soft X-Ray*

There seems to be a connection between absorption in ultraviolet transitions (in particular C IV $\lambda\lambda$1548.204,1550.781) and "warm absorbers" in the soft X-rays (e.g., from O VII, and O VIII edges) from both studies of statistical coincidence (e.g., Brandt et al. 2000; Monier et al. 2001) and from analyses of specific sight lines (e.g., Scott et al. 2004b; Crenshaw et al. 2003; Gabel et al. 2003a, 2003b; Mathur et al. 1995). Since the absorption in these two bands results from species with widely differing ionization potential, the precise causal connection is unclear. HE 0226−4110 was detected by the *ROSAT* All-Sky Survey (RASS; Voges et al. 1999) with a count rate of 0.56 ± 0.06 counts s^{-1} in the 0.2–2.0 keV bandpass of the PSPC. Grupe et al. 1998 fit the RASS PSPC X-ray spectrum of HE 0226−4110 assuming the intrinsic spectrum is a single power law and reported a best-fit spectral index of $\alpha_{\rm X} = -2.1 \pm 0.0.2$ with a total absorbing column density of $N({\rm H}) = (1.78 \pm 1.2) \times 10^{20}$ cm^{-2}. The origin of this total absorbing column density can be attributed to Galactic absorption. (From a fit to damped Lyα and Lyβ lines, Fox et al. [2005] find a Galactic H I column density of $1.2^{+0.4}_{-0.3} \times 10^{20}$ cm^{-2}. Similarly, Wakker et al. [2003] report an H I column density of $1.55 \pm 0.01 \times 10^{20}$ cm^{-2} from a fit to 21 cm emission in this direction.) Grupe et al. (1998) find no evidence for a significant amount of the absorption in the soft X-rays, and in particular from O VII and O VIII.

In further characterizing the ionizing radiation field, we compute the two-point 2 keV to 2500 Å spectral index, $\alpha_{\rm ox}$, which provides a measure of the relative importance of the X-ray emission to the UV emission. Using our power-law fit to the STIS spectrum and the Grupe et al. (1998) power-law fit to the *ROSAT* spectrum, we find $\alpha_{\rm ox} = -1.46 \pm 0.04$, which is close to the average value for unabsorbed quasars ($\langle \alpha_{\rm ox} \rangle \approx -1.5$; Brandt et al. 2000).

4. ASSOCIATED ABSORBER PROPERTIES AT $z_{\rm abs} = 0.4925$

For associated absorption, our *HST* STIS and *FUSE* spectra the spectra cover the rest-frame wavelength range 610–1140 Å. In this range, we detect absorption at $z_{\rm abs} = 0.4925$ in H I Lyβ, Lyγ, Lyδ, C III λ977.020, N IV λ765.148, O III λ832.927, O IV λ787.711, O V λ629.730, O VI $\lambda\lambda$1031.926, 1037.617, Ne VIII λ770.409, and S IV λ748.400. Other transitions, notably C II λ1036.337, O I λ877.879, and O II $\lambda\lambda$834.466, 833.329 are also covered in our spectrum, but are not detected. O III λ702.332 is also covered by our spectrum and has a line strength that is larger than the 832.927 Å transition, but it is blended with Galactic Ar I λ1048.220. (For this study, we adopt transition wavelengths and oscillator strengths from Morton [2003] for transitions above 912 Å, and from Verner et al. [1994] for transitions below 912 Å.) In Figure 5 we plot the detected transitions (*histogram*) in velocity with $z_{\rm abs} = 0.4925$ defining the velocity zero point. (Integration of the O III λ832.927 line yields a centroid redshift of $z_{\rm abs} = 0.49246 \pm 0.00006$. Henceforth, all quoted velocities are referenced to $z_{\rm abs} = 0.4925$.) The smooth curves overplotted on the data indicate our estimated continua obtained by fitting a low-order ($\leq$5) Legendre polynomial to the adjoining continuum regions. These continuum fits follow the formalism described by Sembach & Savage (1992).

We make two remarks regarding the continuum fits to the O III λ832.927 and Ne VIII λ770.409 lines. Inspection of the continuum fit to the O III λ832.927 lines shows several bins blueward of the absorption profile [corresponding to the velocity range $-100 \leq v({\rm km\ s^{-1}}) \leq -50$] that appear above the continuum. In order to fit these bins and lower them to the continuum level, we would require an polynomial order of at least 7, larger than what is prescribed by Sembach & Savage (1992). Using such a high order, we would be in danger of fitting out some of the absorption. Outside of the velocity range $-100 \leq v({\rm km\ s^{-1}}) \leq +5$ the fit appears quite good. In addition, the fit to the broad and shallow trough of the Ne VIII λ770.409 is not well represented in the expand view of Figure 5. We refer the reader to the bottom left panel of Figure 2, where we show a larger wavelength range with the Legendre-polynomial fit to the local continuum superimposed. The continuum placement is reasonable.

In order to remove biases due to transition strengths ($\log f\lambda$) and compare profiles of species on a common (and physically meaningful) scale, we transform the flux profiles of each detected transition into apparent column density profiles using the method described by Savage & Sembach (1991).

$$N_a(v) = \frac{m_e c}{\pi e^2} \frac{1}{f\lambda_0} \ln \left[\frac{I_c(v)}{I(v)} \right], \qquad (2)$$

where f and λ are the oscillator strength and rest wavelength of the transition, and $I_c(v)$ and $I(v)$ are the continuum and attenuated fluxes, respectively. These are shown in Figure 6. Apparent column density profiles from multiple transitions from a given species are useful in testing for unresolved saturated structure, blends with transitions of other species from other absorption-line systems, and for assessing the levels of unocculted flux (e.g., scattered light within the instrument, or elevated background levels). For systems that are potentially intrinsic to the quasar, apparent column density profiles provide a means of assessing the fraction(s) of the quasar continuum/emission-line region that is occulted by the absorbing gas (e.g., Scott et al. 2004b; Ganguly et al. 1999; Hamann et al. 1997b; Barlow & Sargent 1997).

For the associated absorption along this sight line, our spectra cover multiple transitions of H I (Lyβ and higher order Lyman series), and O VI (the resonant doublet $\lambda\lambda$1031.927,1037.617). In Figure 6 we overlay the apparent column density profiles of the O VI doublet (*left side, bottom panel*). The apparent excess of column density in the O VI λ1037.617 transition over the relative velocity range $-120 \leq v({\rm km\ s^{-1}}) \leq 0$ is due to Galactic and high-velocity cloud absorption by the C IV λ1548.204 line (Fox et al. 2005). At all other velocities, the O VI λ1031.927 and λ1037.617 lines are in excellent agreement (within the errors) and there is no evidence for unresolved saturated structure, or for partial coverage of the quasar continuum/broad emission line region. Also, strongly saturated lines such as C III λ977.020 are black in the line core (i.e., no flux is significantly detected), which further indicates that the absorber fully covers the continuum flux source.

There is a weak intervening IGM Lyα line at $z_{\rm abs} = 0.19374$ (Lehner et al. 2006) that is blended with the Lyγ line from the associated absorber at $v \sim -65$ km s^{-1}. The intervening Lyα line appears somewhat broad and shallow, and the Lyγ line of the associated absorber lies on its wing. Due the noisiness of the data on the blue wing of the $z = 0.19374$ Lyα line, it is difficult to assess its contribution to the $z = 0.4925$ Lyγ profile and the level

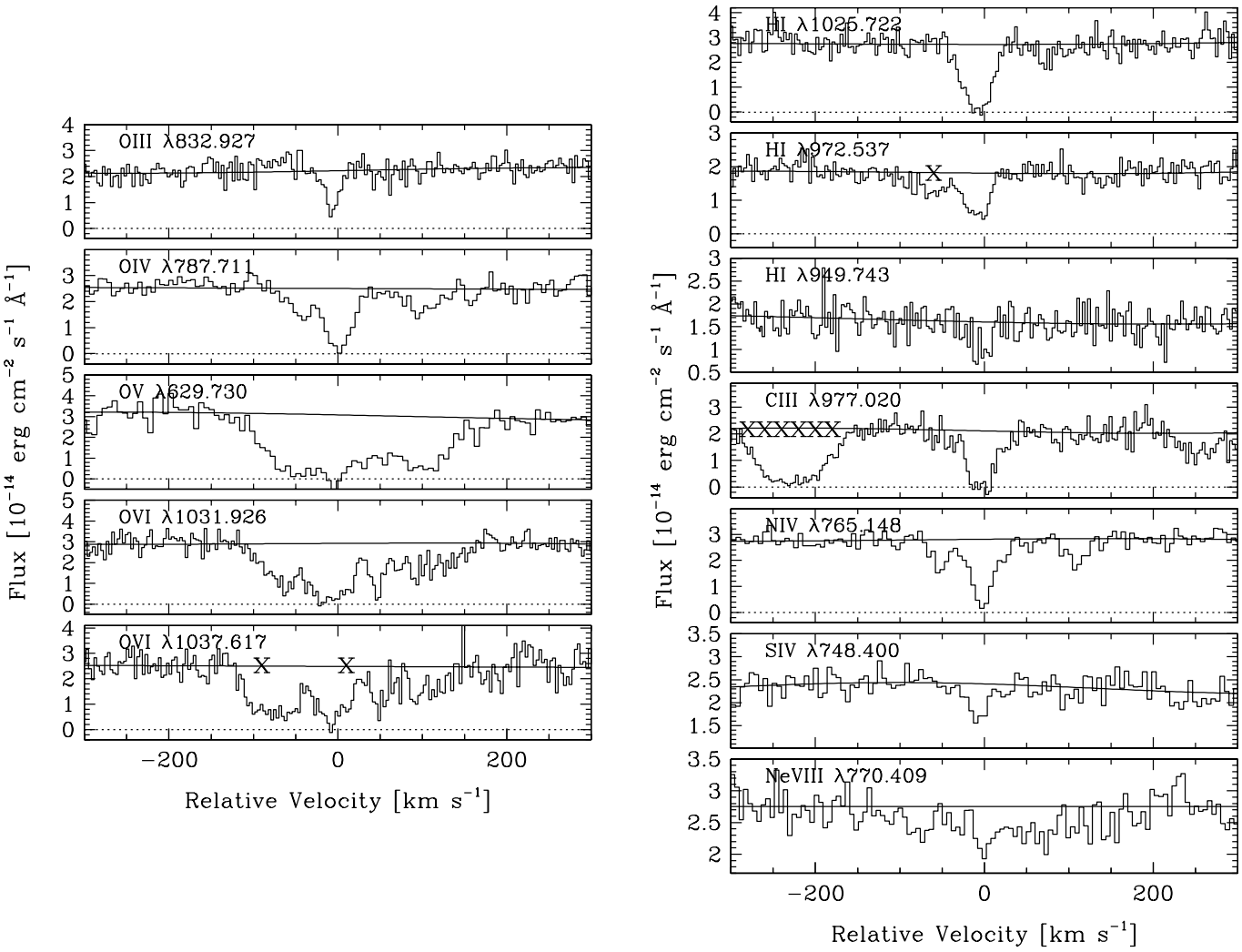

FIG. 5.—Plots of flux vs. velocity (relative to $z_{abs} = 0.4925$) of ions detected in the *FUSE* and STIS spectra. Velocities where absorption is blended by a feature from an unrelated system are marked with a cross. The smooth curves are our assessment of the local continuum using low-order Legendre polynomials. On the left, we plot all detected transitions from species of oxygen, which clearly show the ionization-dependent differences in the kinematics. On the right, we show transitions from all other detected species. Due to the shallowness of the Ne VIII λ770.409 absorption, the profile and continuum fit are not well represented in this expanded velocity range. We refer the reader to the bottom left panel of Fig. 2 for a better view of this absorption profile and its continuum fit. [*See the electronic edition of the Journal for a color version of this figure.*]

of saturation in the core of the Lyβ. (The Lyδ line is detected, but is also too noisy for this purpose.) We return to this issue in § 4.1 by using the O III λ832.926 profile. We note here that Lehner et al. (2006) report $\log N(\text{H I})(\text{cm}^{-2}) = 13.20 \pm 0.06$ and $b(\text{H I}) = 28.7 \pm 6.0$ km s^{-1} for the intervening $z_{abs} = 0.19374$ Lyα line.

We make one final note regarding the apparent column density profiles as a whole before continuing with more detailed investigations of the various components. The rest-frame transitions in the 732–792 Å wavelength range lie in both the LiF1B and LiF2A detector segments of the *FUSE* spectra. We overlay the apparent column density profiles from both channels for the S IV λ748.400 (Fig. 6, *right side, bottom right panel*), N IV λ765.148 (Fig. 6, *right side, middle panel*), and O IV λ787.711 (Fig. 6, *left side, second panel from the top*) lines. The agreement between the LiF1B and LiF2A profiles for N IV and S IV is excellent. For the O IV profiles, there is a discrepancy in the bins near 0 km s^{-1} where the line profile reaches zero flux. The profiles are in excellent agreement otherwise, and we have no reason to suspect either one. We attribute the discrepancy near 0 km s^{-1} to Poisson errors, and use the profiles from the LiF2A detector segment for our investigation below (due the higher signal-to-noise ratio). The excellent agreement evident in Figure 6 indicates that the LiF1 and LiF2 channels have very similar spectral resolutions.

4.1. *Narrow Components*

4.1.1. *Low- and Moderate-Ionization Gas at* $v = -8$ km s^{-1} (*in the* $z = 0.4925$ *Rest Frame*)

In Figures 5 and 6, absorption is clearly detected at −8 km s^{-1} in a wide variety of ionization species, from neutral H I, to low-ionization C III and O III, to moderate-ionization N IV, O IV, S IV, to high-ionization O V, O VI and Ne VIII. The kinematics of the absorption at this velocity is complex (and possibly multiphase). Neutral (H I) and low-ionization species (C III, O III) appear as a discrete feature over the velocity range $-30 \leq v(\text{km s}^{-1}) \leq +5$, while the higher ionization species (N IV, O IV) appear as a broader feature over the velocity range $-30 \leq v(\text{km s}^{-1}) \leq +30$. The more highly ionized species (O V–VI, Ne VIII) appear absorbed with little substructure over the entire velocity range $-30 \leq v(\text{km s}^{-1}) \leq +30$, not as a single discrete feature. We focus here

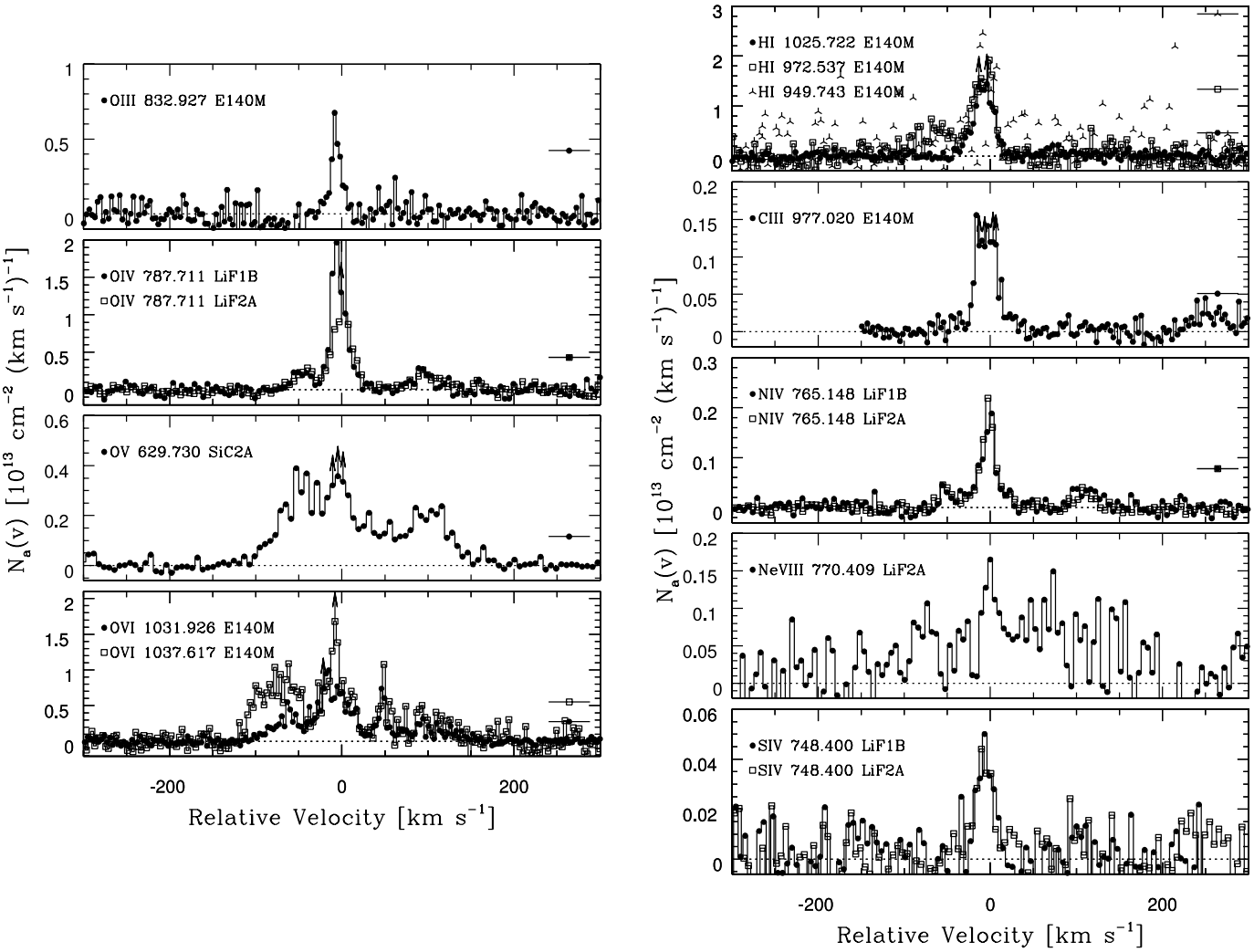

FIG. 6.—Apparent column density profiles of the detected species as a function of velocity relative to $z_{abs} = 0.4925$. Transitions from a given species are overplotted in the same panel. A horizontal bar on the right side of each panel marks the apparent column density where each transition reaches unit optical depth. *FUSE* data are shown with a sampling of three bins per resolution element, while STIS data are shown with a sampling of two bins per resolution element. Species of oxygen are plotted on the left, while other species are plotted on the right. [*See the electronic edition of the Journal for a color version of this figure.*]

on the discrete features appearing in the H I, C III, N IV, O III–IV, and S IV ions.

To investigate the number of phases that are required to explain the absorption at -8 km s^{-1} and the ionization conditions of each phase, we first overlay the apparent column density profiles of the neutral, low- and moderate-ionization species in Figure 7. In the left panels of Figure 7, we overplot the H I and C III apparent column density profiles on top of the O III profile. For H I, we use the Lyβ profile because it provides the best and cleanest information in the shapes of the wings without suffering from blends (as in the case of Lyγ) or noise (as in the case of Lyδ). We comment on this further below. The kinematics of these species is remarkably similar and suggest an origin in the same phase. (Note the gradual trend toward increasing column density in the velocity range $-30 \leq v \leq -15$ km s^{-1}, and the sharp drop-off at 5 km s^{-1}.) The reason for this asymmetry is unclear. If the absorption results from the superposition of symmetric (e.g., Gaussian) profiles, then at least two such components are needed to reproduce the observed profile. However, it is not clear that such an assumption is required (e.g., Ganguly et al. 2005; Arav et al. 2002). Regardless, if the kinematics of the H I and C III in the velocity range $-15 \leq v \leq +5$ km s^{-1} are also well traced by the O III profile, we can use the O III profile as a template to estimate the level of saturation, and, more importantly, to obtain column density ratios to constrain the ionization conditions of the low-ionization phase. We summarize these ratios below.

In the right panels of Figure 7, we overplot the O IV, N IV, and S IV profiles on top the O III profile. These overlays also show that the kinematics of these profiles do not match that of the O III profile. They are wider, possibly resulting from a blend of different kinematic components (see § 4.1.2. With the simple assumption that any O IV, N IV, and S IV that coexists in the O III–bearing gas have the same kinematic profile, we can place limits on how much of these higher ionization species relative to O III could arise in that phase (in the interest of providing the most information to constrain ionization models). (Although there is no apparent shift in the centroid of S IV λ784.400 line relative to the O III λ832.927 line, the kinematics of the two profiles do not match. While it is possible that this could be an effect of the resolution, since the S IV λ784.400 line appears in the *FUSE* LiF2 channel, the profile spans over three resolution elements. Thus, we

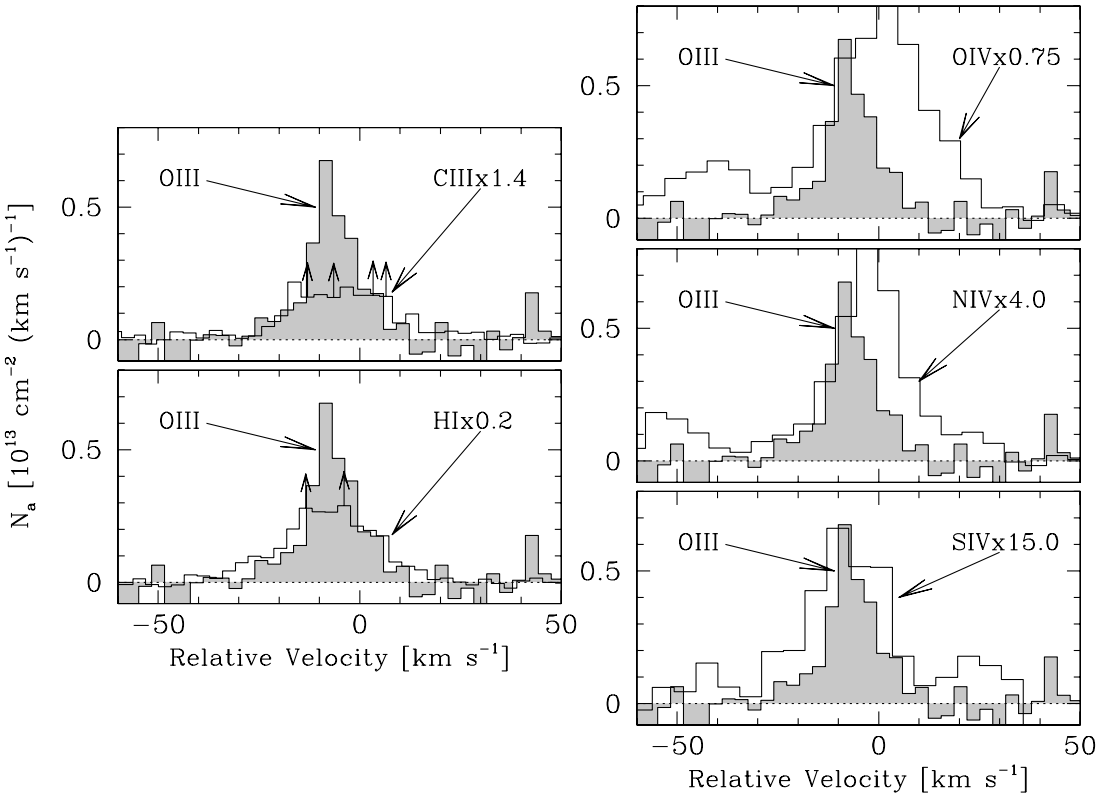

FIG. 7.—O III apparent column density profiles *(shaded histograms)* overlaid on the H I, C III, N IV, O IV, and S IV apparent column density profiles. Vertical arrows are shown for pixels where the flux is negative due to Poisson fluctuations at low flux levels. The H I and C III profiles are scaled to match the O III profile in unsaturated regions. The N IV and O IV profiles are scaled to match the blue wing of the O III profile. The S IV profile is scaled to match the peak of the O III profile. [*See the electronic edition of the Journal for a color version of this figure.*]

report only a limit on the N(S IV)/N(O III) ratio.) In Figure 7, we use the O III profile, which appears over the velocity range $-30 \leq v(\mathrm{km\ s^{-1}}) \leq +5$, to estimate the following constraints on the column density ratios for the O III–bearing gas:

$$\begin{aligned} N(\mathrm{H\ I})/N(\mathrm{O\ III}) &\approx 5, \\ N(\mathrm{C\ III})/N(\mathrm{O\ III}) &\approx 0.74, \\ N(\mathrm{N\ IV})/N(\mathrm{O\ III}) &\lesssim 0.25, \\ N(\mathrm{O\ IV})/N(\mathrm{O\ III}) &\lesssim 1.3, \\ N(\mathrm{S\ IV})/N(\mathrm{O\ III}) &\lesssim 0.07. \end{aligned} \quad (3)$$

In the columns (4) and (5) of Table 2, we report our equivalent width measurements and further summarize our column density assessments of the O III–bearing gas using the above ratios. Direct integration of the O III profile over the above velocity range yields a column density of $N_a(\mathrm{O\ III}) = (8.4 \pm 1.1^{+0.5}_{-1.7}) \times 10^{13}$ cm^{-2}, where the first error is the 1 σ confidence error resulting from statistical and continuum placement uncertainties and the latter error is the systematic uncertainty resulting from the choice of integration range. (To assess this latter error, we added and subtracted 10 km s^{-1} to the integration range.) We note that the resulting H I column density implied by equation (3) [$N(\mathrm{H\ I}) \approx (4.2 \pm 0.6^{+0.3}_{-0.9}) \times 10^{14}$ cm^{-2}] is consistent with the curve of growth of the Lyman series equivalent widths. In addition, we integrated the region of the spectrum where the O II λ833.329 line ($\log f\lambda = 2.097$) is expected and find a limiting column density of $N(\mathrm{O\ II}) < 1.3 \times 10^{13}$ cm^{-2} (3 σ) for this low-ionization phase.

To understand the ionization structure of the O III–bearing phase, we assume that the absorption arises from a photoionized plane-parallel slab with a solar relative abundance pattern [n(C)/n(O) = 0.537; Asplund et al. 2005 and references therein] and use the above column density ratios to infer the ionization parameter, U, defined as the number density of ionizing photons per baryon, and metallicity, [O/H]. We use the CLOUDY photoionization code (Ferland et al. 1998) to compute the best-fit model, specifying the radiation field as an AGN spectrum with the following parameters (as described in § 3): $T = 15{,}000$ K, $\alpha_{\mathrm{ox}} = -1.46$, $\alpha_{\mathrm{UV}} = -0.58$, $\alpha_x = -2.1$, normalized to $\log L_\nu(1\ \mathrm{ryd}) = 30.65$. (See § 3 for a justification of these parameters.) In Figure 8 we show χ^2 contours on the [O/H]-U plane. The best fitting parameters are

$$\begin{aligned} [\mathrm{O/H}] &= +0.12^{+0.16}_{-0.03}, \\ \log U &= -2.29^{+0.02}_{-0.23}, \\ \log N(\mathrm{H}) &= 17.54^{+0.04}_{-0.25}. \end{aligned} \quad (4)$$

The total hydrogen column density of the O III–bearing phase results from a combination of the integrated O III column density (Table 2), the H I/O III column density ratio from equation (3), and the H I ion fraction implied by the ionization parameter: $N(\mathrm{H}) = N(\mathrm{O\ III}) \times [N(\mathrm{H\ I})/N(\mathrm{O\ III})] \times f_{\mathrm{HI}}^{-1}(U)$. The ionization parameter is most tightly constrained by the O IV/O III limit and C III/O III (with the assumed solar relative C/O abundance) ratio.

Increasing the carbon to oxygen relative abundance to [C/O] = +0.1 yields a slightly better fit to the observations (best parameters: [O/H] $\sim +0.45$, $\log U \sim -2.73$), since the lower constraint on the ionization parameter provided by C III/O III is relaxed. The best-fit model presented above yields O IV/O III at the observational limit, while the [C/O] = +0.1 best-fit model predicts O IV/O III well below the limit. (The CLOUDY model produces a factor of

TABLE 2
INTEGRATION OVER NARROW COMPONENTS (IN THE $z_{abs} = 0.4925$ REST FRAME)

			$-30 \le v(\mathrm{km\ s^{-1}}) \le +5$		$-30 \le v(\mathrm{km\ s^{-1}}) \le +30$		$+30 \le v(\mathrm{km\ s^{-1}}) \le +60$	
Ion (1)	Wavelength[a] (Å) (2)	$\log f\lambda$[a] (3)	W_λ (mÅ) (4)	N_a[b,c] (10^{13} cm^{-2}) (5)	W_λ (mÅ) (6)	N_a (10^{13} cm^{-2}) (7)	W_λ (mÅ) (8)	N_a[d] (10^{13} cm^{-2}) (9)
H I	1025.722	1.909	149 ± 4	≈ 42	...	...	<21	<1.8
	972.537	1.450	101 ± 5	...	...	...	...	...
	949.743	1.122	48 ± 8	...	...	...	...	...
C III	977.020	2.869	125 ± 7	≈ 6.2	...	...	<26	<0.26
N IV	765.148	2.684	...	$\lesssim 2.1$	119 ± 4	4.6 ± 0.3	<12	<0.26
O I	877.879	1.714	<19	<2.8	...	...	<17	<2.8
O II	833.329	2.097	<20	<1.3	...	...	<19	<1.2
O III	832.927	1.950	54 ± 5	8.4 ± 1.1	...	...	<18	<1.9
O IV	787.711	1.942	...	$\lesssim 11$	142 ± 5	36 ± 3	<15	<1.8
O V	629.730	2.511	...	...	164 ± 4	15 ± 2	66 ± 4	$\lesssim 2.9$
O VI	1031.926	2.136	...	...	238 ± 6	31 ± 2	88 ± 5	8.7 ± 1.2
Ne VIII	770.409	1.908	...	...	36 ± 6	5 ± 0.8	17 ± 4	$\lesssim 1.8$
S IV	748.400	2.573	...	$\lesssim 0.56$	28 ± 6	0.9 ± 0.2	<14	<0.35

NOTE.—Errors on all quantities are quoted at 1 σ confidence. Upper limits are quoted at 3 σ confidence. The velocity range is quoted in km s^{-1} relative to $z_{abs} = 0.4925$.

[a] Atomic data for transitions above the Lyman limit at 912 Å were taken from Morton (2003). For transitions blueward of the Lyman limit, we use data compiled by Verner et al. (1994).

[b] The column densities for H I and C III were determined using the integrated column density from the O III λ832.927 profile and the column density ratios in Fig. 7.

[c] The column density limits for N IV , O IV, and S IV were determined using the integrated column density from the O III λ832.927 profile and the column density limits in Fig. 7.

[d] The column density limits for O V and Ne VIII were determined using the integrated column density from the O VI 1037.617 Å profiles and the limiting column density ratios in Fig. 10.

1.3 less N IV column density than the observational limit.) All other best-fit models with nonsolar carbon to oxygen abundances ([C/O] > 0.1, [C/O] < 0) fail to reconcile the O III column density and C III/O III column density ratio. (Photoionization models with [C/O] > 0.1 predict ratios that are too large; those with [C/O] < 0 predict ratios that are too small.) Such an enhancement may be reasonable given that the Fe/α relative abundance appears to be enhanced in the emission-line regions of AGNs (e.g., Hamann & Ferland 1999 and references therein). There is evidence from the atmospheres of Galactic halo stars (e.g., McWilliam 1997) that the C/Fe is roughly constant (at the solar value) over a large range in metallicity. If this insensitivity can be extrapolated to the supersolar metallicities of AGN line-emitting regions, then a slightly supersolar C/O relative abundance in this $z_{abs} \sim 0.5$ absorber is reasonable.

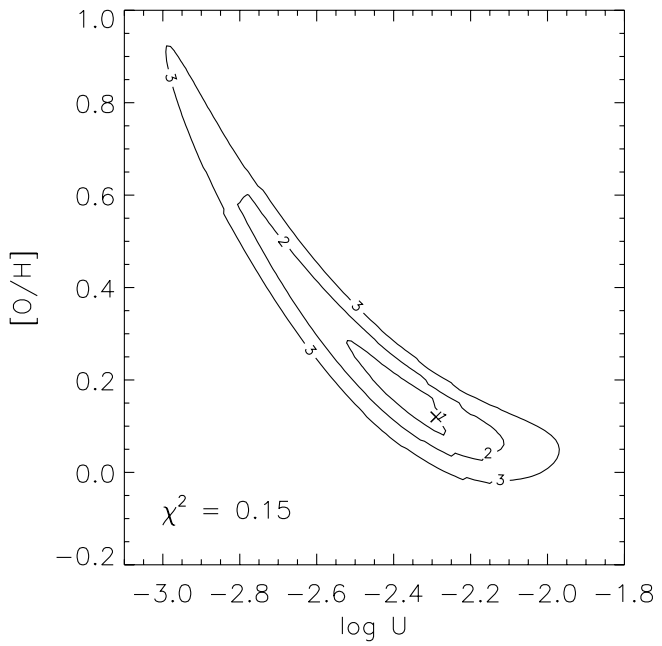

FIG. 8.—Plot shows the $\Delta\chi^2$ contours on the metallicity ([O/H])-ionization parameter (U) plane for the low-ionization phase of the $v = -8$ km s^{-1} component probing the narrow emission line region. The optimal parameters are marked with a cross, while contours are drawn for 1, 2, and 3 σ confidence regions.

We note here that the ionization fractions of O V and O VI for the O III–bearing gas are 6.75×10^{-2} and 2.52×10^{-3}, respectively, compared to 0.4 for O III. This implies column densities of N(O V) $\sim 10^{13}$ cm^{-2}, and N(O VI) $\sim 5 \times 10^{11}$ cm^{-2}. Integration of the O V and O VI over the velocity range $-30 \le v(\mathrm{km\ s^{-1}}) \le +5$ yield apparent column densities of N_a(O V) $= (1.1 \pm 0.1) \times 10^{14}$ cm^{-2}, and N_a(O VI) $= (2.4 \pm 0.4) \times 10^{14}$ cm^{-2}. These high-ionization species must arise in a phase/component of gas that is separate from the O III–bearing gas.

4.1.2. *Moderate- and High-Ionization Gas at $v = 0$ km s^{-1} (in the $z = 0.4925$ Rest Frame)*

As we pointed out in the previous section from the overlays of the O IV, N IV, and S IV apparent column density profiles on top of the O III profile, we can only place limits on the amount of higher ionization species that coexists in the O III–bearing gas. We return to the issue of the higher ionization species here. These higher ionization species appear over the velocity range $-30 \le v(\mathrm{km\ s^{-1}}) \le +30$. In columns (6) and (7) of Table 2 we report equivalent width and apparent column density integrations of these and high-ionization species (O V–VI, Ne VIII) over this velocity range. (We do not report additional measurements of H I, C III, or O III as there is no additional information over that reported in cols. [4] and [5].)

As we pointed out earlier, there are differences in the apparent velocity widths of the O IV, N IV, and S IV compared to O III, H I,

and C III. There are two additional aspects of Figure 7 that merit consideration. First, there is a $\sim$+8 km s^{-1} velocity shift in the peak of the O IV and N IV profiles relative to the O III profile. Second, in the velocity range $+5 \leq v \leq +30$ km s^{-1}, there is significant column density apparent in O IV, whereas none exists in the O III, H I, and C III profiles.

From this we conclude that there is at least one additional higher ionization phase of gas at these velocities which produces O IV, N IV, and possibly some O V, and O VI. This "component" is not necessarily restricted to the velocity range $+5 \leq v(\text{km s}^{-1}) \leq +30$, however. It is certainly plausible that the absorption by this gas extends down to velocities where the O III–bearing gas appears. (For this reason, we can only quote limits on the column density ratios in the previous section.) In fact, as mentioned in the previous section, additional gas in the velocity range common with that of the O III–bearing gas [i.e., $-30 \leq v(\text{km s}^{-1}) \leq +5$] is required to explain the column densities of the high-ionization species O V–VI.

Since much of the O IV and N IV column density in the velocity range $-30 \leq v(\text{km s}^{-1}) \leq +5$ can be explained by the O III–bearing gas, we focus here on the remaining velocity range $+5 \leq v(\text{km s}^{-1}) \leq +30$ (with the aforementioned caveats). In Figure 9 we compare the apparent column density profiles of O V–VI and N IV to that of O IV. In the velocity range $+5 \leq v(\text{km s}^{-1}) \leq +30$, there is good agreement between the kinematics of O IV and N IV, so the two likely coexist in the same phase of gas. (Note that the N IV profile has been scaled vertically.) Figure 9 also shows that the kinematics of O V–VI do not match O IV in the velocity range $+5 \leq v(\text{km s}^{-1}) \leq +30$. This implies that the absorbing gas of those two species at these velocities arise in a separate phase/component (probably one of the broad components described in § 4.2). Using the comparison of the apparent column density profiles we can still place limits on how much O V–VI could arise in the O IV–bearing gas at these velocities. (Here, we again make the simple assumption that any O V–VI that coexists in the O IV–bearing gas must have the same kinematics as the O IV over those velocities.) We find the following constraints:

$$N(\text{N IV})/N(\text{O IV}) \approx 0.1,$$
$$N(\text{O V})/N(\text{O IV}) \lesssim 0.32,$$
$$N(\text{O VI})/N(\text{O IV}) \lesssim 0.53. \quad (5)$$

For the O IV–bearing gas in the velocity range $+5 \leq v(\text{km s}^{-1}) \leq +30$, we find N_a(N IV)/N_a(O IV) $\approx$ 0.1 (compared to $\approx$0.2 for the CLOUDY model of the O III–bearing gas). In the photoionization models described above, the smallest achievable N(N IV)/N(O IV) ratio is $\approx$0.14, which occurs at an ionization parameter of $\log U \approx -2.6$. This is problematic for two reasons. First, at this ionization level, we would expect to see O III at these velocities, which we do not (see Figs. 6 and 7) down to a 3 σ confidence limit of 1.6×10^{13} cm^{-2}. Second, while the ratio is close, this ionization level does not really explain the observed ratio. There are two possible conclusions from this simple analysis. Either pure photoionization by the quasar may be the only ionization mechanism for the O IV/N IV–bearing gas at these velocities, or the N/O relative abundance deviates from our assumed solar ratio (N/O = 0.132, Asplund et al. 2005).

If the ionization mechanism of this gas is predominantly photoionization by the quasar, then the lack of O III implies that the ionization parameter must be larger than $\log U \approx -1.7$. At this ionization level, and with solar relative abundances, the N IV/O IV ratio is $\approx$0.17. Thus, the N/O abundance must be lowered by at least $\approx$0.07 dex relative to the solar value (i.e., [N/O] $\lesssim -0.07$) to match the observed N IV/O IV ratio.

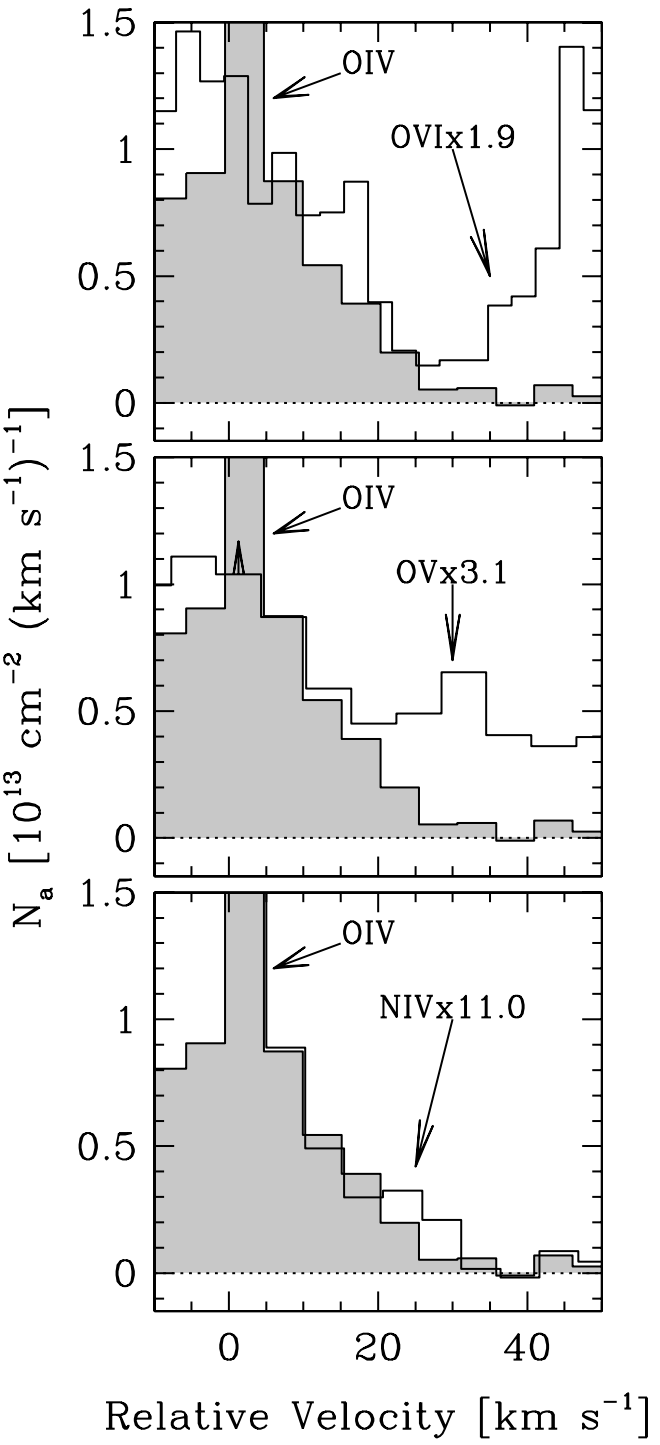

FIG. 9.—Apparent column density profile of O IV (*shaded histogram*) overlaid on the O VI (*top*), O V (*middle*), and N IV (*bottom*) profiles (*unshaded histograms*) in the region of the $v = 0$ km s^{-1} component. The N IV profile has been scaled to match the O IV profile in the velocity range $+5 \leq v(\text{km s}^{-1}) \leq +30$. The O V–VI profiles have been scaled to the minimum allowable value to hide the O IV profile in that same velocity range. [*See the electronic edition of the Journal for a color version of this figure.*]

4.1.3. *High-Ionization Gas at* $v = +50$ km s^{-1} (*in the* $z = 0.4925$ *Rest Frame*)

In Figures 5 and 6 there is clearly a narrow component detected in O VI at +50 km s^{-1} in the $z = 0.4925$ rest frame. This component is not detected in any low- to moderate-ionization species (i.e., H I, C III, N IV, O III, O IV, S IV). Absorption is detected at this velocity in O V and Ne VIII. However, it appears that those species

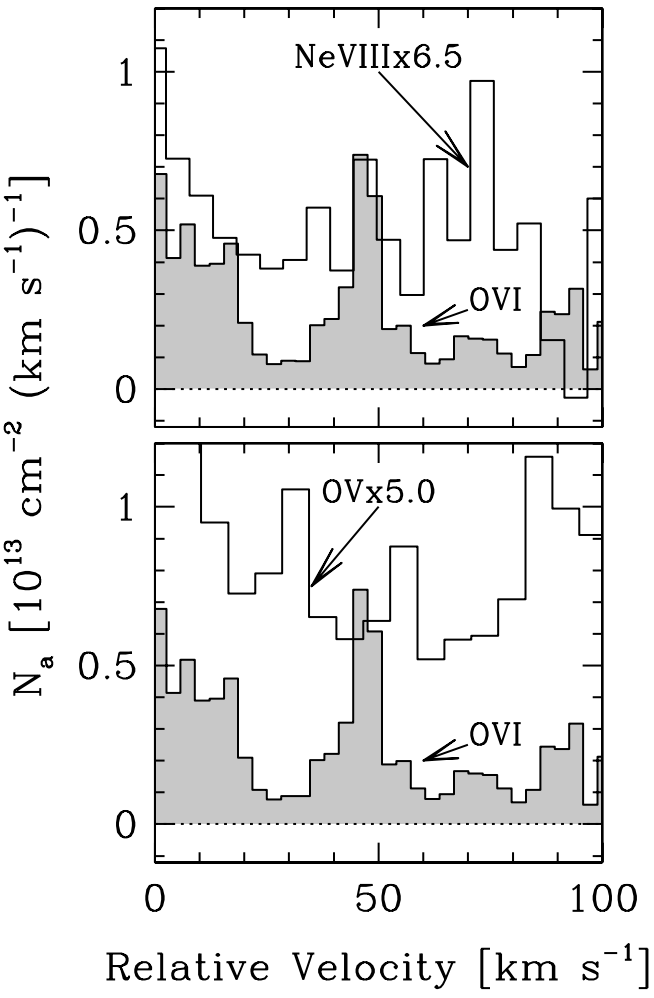

FIG. 10.—Apparent column density profile of O VI (*shaded histogram*) overlaid on the O V (*bottom*) and Ne VIII (*top*) profiles (*unshaded histograms*) in the region of the $v = +50$ km s^{-1} component. The O V and Ne VIII profiles have been scaled to the minimum allowable value to hide the O VI profile. [*See the electronic edition of the Journal for a color version of this figure.*]

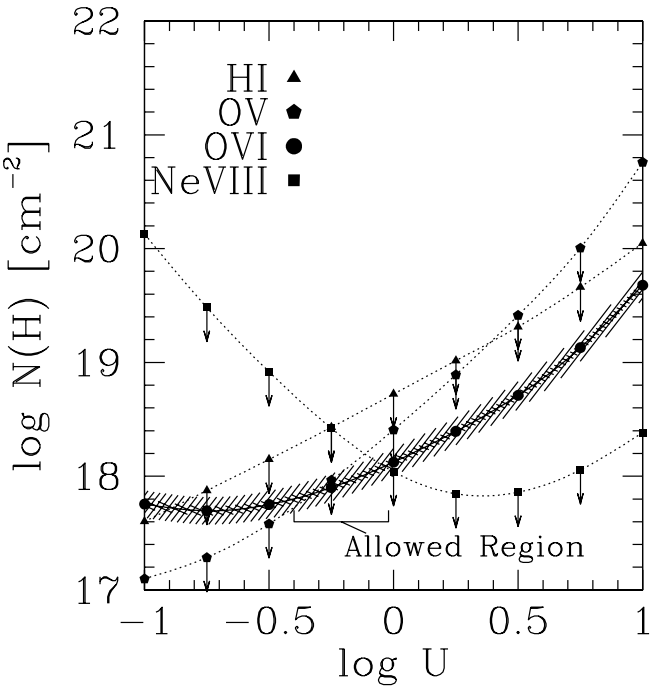

FIG. 11.—Isopleths of species column density in total column density [N(H)] ionization parameter (U) space for the $v = +50$ km s^{-1} component. The relevant species for each curve is distinguished by the symbols shown in the corner. For O VI, the hatched regions around the curve indicate the 1 and 3 σ confidence uncertainties. For all other species, the curves are shown as upper limits. The region of parameter space that satisfies all column density information is marked "allowed region." The models assumed a metallicity [O/H] = +0.12, with solar relative abundances. [*See the electronic edition of the Journal for a color version of this figure.*]

arise from the broader component at $v \sim 100$ km s^{-1}. If so, the only ion detected in this narrow component is O VI. To place constraints on the column densities of species (for the consideration of ionization models below), we integrate the apparent column density profiles of nondetected species and O VI over the velocity range $+30 \leq v \leq +60$ km s^{-1}. For O V and Ne VIII, we take the same approach as in the previous section and consider how much of the absorption observed in this velocity range could be attributed to the O VI component. In Figure 10 we plot the O VI apparent column density profile over those of O V (*bottom panel*) and Ne VIII (*top panel*). In each case, we have scaled the apparent column density profile to match the level of the O VI. This yields the following constraints:

$$N(\text{O V})/N(\text{O VI}) \lesssim 0.2, \quad (6)$$
$$N(\text{Ne VIII})/N(\text{O VI}) \lesssim 0.15.$$

In columns (8) and (9) of Table 2, we summarize our equivalent width measurements [over the velocity range $+30 \leq v(\text{km s}^{-1}) \leq +60$] and column density constraints.

The velocity width of O VI ($b = 9 \pm 1$ km s^{-1})[7] implies a maximum temperature of $\log T(\text{K}) \leq 4.9$. At this temperature collisional processes do not produce appreciable amounts of O VI, so this high-ionization gas likely arises from photoionization. The central engine is likely to dominate the radiation field, so we use the same ionizing spectrum and range of ionization parameters used in the previous two sections. The location of the gas is not clear since there is no additional information (such as a velocity coincidence with a line-emitting region, or a density diagnostic). As a result there is fundamental uncertainty in the metallicity of the gas and, by consequence, the total hydrogen column density. [Since H I is not detected down to $N(\text{H I}) < 1.8 \times 10^{13}$ cm^{-2} (see Table 2), we do not have a means of inferring the metallicity. We can constrain the metallicity only with a model for the ionization, and we return to this below.] To place ionization constraints on the gas, we ran a grid of CLOUDY models over a range of ionization parameters ($-1 \leq \log U \leq 1$) using the same ionizing spectrum and metallicity ([O/H] = 0.12) as in the previous section for the O III phase.

For each species, we generated a curve of total hydrogen column density (as a function of ionization parameter), which reproduces the observed species column density (or limit). The most constraining curves (those for H I, O V, O VI, and Ne VIII) are shown in Figure 11. The shapes of the curves are determined by the ionization fraction of the species, with the minimum in each curve occurring at the ionization parameter that maximizes that species. The relative vertical placements of the curves are determined by the relative abundances of the elements (which are assumed to be solar in these models) except for H I. If the gas can be described by single photoionized phase, then there must be a location (or region) on the N(H)-U plane that satisfies all column density measurements and

[7] This b-value was obtained by taking the second moment of the apparent optical depth distribution over the velocity range $+30 \leq v(\text{km s}^{-1}) \leq +60$.

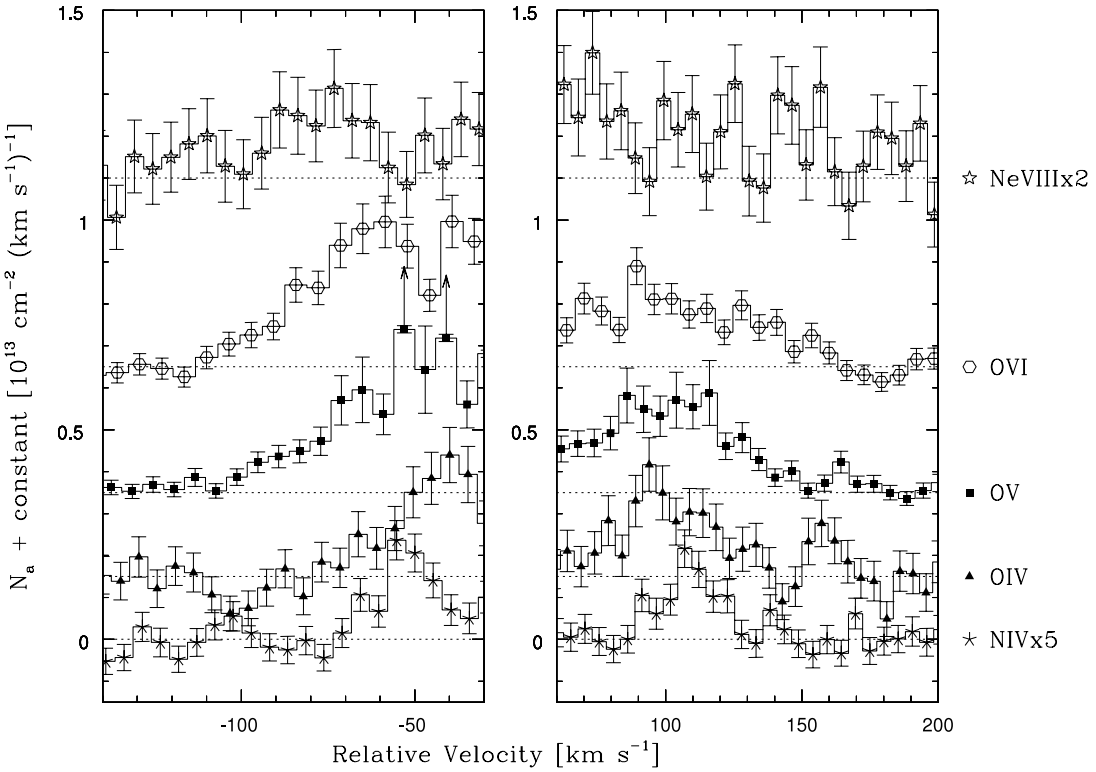

FIG. 12.—Velocity-aligned apparent column density profiles of the N IV, O IV–VI, and Ne VIII ions overlaid on the blue and red wings (*left and right panels, respectively*) of the associated absorber. For purposes of clarity, the profiles are offset vertically, with the "zero level" for each profile shown as a horizontal dotted line. The O VI profiles are shown with a sampling of 7 km s^{-1} per bin, similar to the sampling the *FUSE* data. In addition, the N IV and Ne VIII profiles are shown with a multiplicative factor to offset the abundance differences relative to oxygen. [*See the electronic edition of the Journal for a color version of this figure.*]

constraints. In the case of this component, such a region does exist:

$$(17.65)17.75 \lesssim \log N(\mathrm{H}) \lesssim 18.1(18.15),$$
$$(-0.45) - 0.35 \lesssim \log U \lesssim -0.02(0). \quad (7)$$

The quoted range reflects the 1 σ confidence uncertainty resulting from the error in N(O VI). The parenthetical numbers indicate the 3 σ confidence range. The lower limit on the ionization parameter is established by the comparison of N(O VI) and the limit on N(O V). This is independent of assumed metallicity or relative abundance. The upper limit arises from comparing the O VI and Ne VIII column densities which relies on the assumed relative Ne/O abundance (taken to be Ne/O = 0.151; Asplund et al. 2004 and references therein). The limits on the ionization parameter are probably not sensitive to the uncertainty in the metallicity since the absorber is optically thin (in spite of the large total hydrogen column density) to the ionizing radiation.

If the derived range of ionization parameter for the gas is accurate, then we can place a lower limit to the metallicity of the gas given the O VI column density and the H I column density nondetection limit via

$$[\mathrm{O/H}] = \log\left[\frac{N(\mathrm{O})}{N(\mathrm{H})}\right] - \log\left[\frac{N(\mathrm{O})}{N(\mathrm{H})}\right]_{\odot} \quad (8)$$
$$= \log\left\{\left[\frac{N(\mathrm{O\ VI})}{N(\mathrm{H\ I})}\right]\left[\frac{f_{\mathrm{O\ VI}}^{-1}(U)}{f_{\mathrm{H\ I}}^{-1}(U)}\right]\right\} + 3.34,$$

where $f(U)$ is the ionization fraction and we have used the Asplund et al. (2004) value for the solar oxygen abundance. The minimum value for $f_{\mathrm{O\ VI}}^{-1}(U)/f_{\mathrm{H\ I}}^{-1}(U)$ arises at the largest allowed ionization parameter. For $\log U \sim -0.02$, this fraction is 2.2×10^{-5}. Using the integrated O VI column density and H I column density limit from Table 2, we find a limiting metallicity of $[\mathrm{O/H}] \geq -0.62$.

For a given absorber density, the N(H) axis can also be interpreted as the thickness of the slab and U as the distance between the absorber and quasar central engine. Using the limiting metallicity, the total hydrogen column density could be as large as $N(\mathrm{H}) \sim 5 \times 10^{18}$ cm^{-2}.

It is noteworthy that over the range of ionization parameters allowed by the column density constraints, the dominant stage of oxygen is O VII. For this component, our models predict O VII column densities in the range $\log N(\mathrm{O\ VII}) = 14.4-14.8$.

4.2. *Broad Components*

On the blue and red wings of the associated absorption-line system, we detect broad components in the higher ionization species: N IV, O IV–VI, and Ne VIII. Neither S IV nor any species with an ionization stage smaller than 4 is detected. In Figure 12 we show overlays of the O IV–VI, N IV, and Ne VIII apparent column density profiles in the velocity ranges $-140 \leq v \leq -20$ km s^{-1} and $+60 \leq v \leq +200$ km s^{-1}. In Table 3 we present measurements (equivalent widths and integrated apparent column densities) of the ions covered by our data over those two velocity ranges.

Obtaining velocity centroids and widths for these components in a nonparametric way using the apparent optical depth method is a difficult task for two reasons. Both of these quantities involve moments of the apparent optical depth and can be greatly affected by the noise when the absorption is relatively weak (e.g., with equivalent width less than 5 times the error), and by the choice of integration range (which itself is affected by the assumed

TABLE 3
INTEGRATION OVER BROAD COMPONENTS (IN THE $z_{abs} = 0.4925$ REST FRAME)

Ion	Transition[a] (Å)	log $f\lambda$[a]	$-140 \le v(\mathrm{km\ s^{-1}}) \le -30$		$+60 \le v(\mathrm{km\ s^{-1}}) \le +200$	
			W_λ (mÅ)	N_a ($\mathrm{cm^{-2}}$)	W_λ (mÅ)	N_a ($\mathrm{cm^{-2}}$)
H I	1025.722	1.909	<44	$<3.5 \times 10^{13}$	<53	$<4.3 \times 10^{13}$
C III	977.020	2.869	<49	$<4.5 \times 10^{12}$	<69	$<5.7 \times 10^{12}$
N IV	765.148	2.684	30 ± 8	$(8.0 \pm 1.7) \times 10^{12}$	40 ± 11	$(9.7 \pm 1.9) \times 10^{12}$
O I	877.879	1.714	<36	$<5.2 \times 10^{13}$	<42	$<5.9 \times 10^{13}$
O II	833.329	2.097	<38	$<2.5 \times 10^{13}$	<46	$<2.7 \times 10^{13}$
O III	832.927	1.950	<42	$<3.4 \times 10^{13}$	<45	$<3.9 \times 10^{13}$
O IV	787.711	1.942	40 ± 10	$(6.0 \pm 1.2) \times 10^{13}$	69 ± 11	$(9.2 \pm 1.4) \times 10^{13}$
O V	629.730	2.511	182 ± 10	$(1.5 \pm 0.2) \times 10^{14}$	206 ± 12	$(1.4 \pm 0.1) \times 10^{14}$
O VI	1031.926	2.136	201 ± 13	$(1.8 \pm 0.1) \times 10^{14}$	171 ± 16	$(1.2 \pm 0.1) \times 10^{14}$
Ne VIII	770.409	1.908	32 ± 8	$(4.2 \pm 1.0) \times 10^{13}$	51 ± 10	$(6.9 \pm 1.2) \times 10^{13}$
S IV	748.400	2.573	<26	$<6.7 \times 10^{12}$	<31	$<7.9 \times 10^{12}$

NOTES.—Errors on all quantities are quoted at 1 σ confidence. Upper limits are quoted at 3 σ confidence.
[a] Atomic data for transitions above the Lyman limit at 912 Å were taken from Morton (2003). For transitions blueward of the Lyman limit, we use data compiled by Verner et al. (1994).

structure of the absorption profile). For O V λ629.73 and O VI λ1031.926, which are the strongest unblended lines in these components, we find $b \sim 23-32$ km s^{-1} for the blue wing and $b \sim 29-40$ km s^{-1} for the red wing using the integration ranges quoted above and in Table 3. These ranges include an assessment of the uncertainty due to the choice of integration range by adding and removing 20 km s^{-1} to the range.

On the red wing, the apparent column density profile of O IV–VI appear to match, at least to within the errors. There is a possible excess of column density in the O V profile at $v = +110$ km s^{-1} over O VI, and an excess of O VI at $v = +140$ km s^{-1} over O IV. The O IV profile is consistent with zero column density at $v = +140$ km s^{-1}. It is not clear whether this indicates an actual termination of the broad component (at a velocity smaller either the O V or O VI) with an additional component at higher velocities, or whether both are actually part of the same component. The similarity of the O V and the O VI profiles (modulo the aforementioned excess) indicates that both are produced in the same gas. It is difficult to place interesting ionization constraints on this phase given the lack of additional information.

On the blue wing, there are clear differences in the kinematics of the O IV profiles compared to O V and O VI, which appear to rule out the production of all three species in the same phase. The O IV profile appears to terminate at $v = -80$ km s^{-1}, with no detectable column density blueward of that velocity. On the other hand, O V and O VI are detected at those velocities and appear to trace each other perfectly at $v \le -90$, with the termination of the profile near $v = -110$ km s^{-1}. In the range $-90 \le v \le -60$ km s^{-1}, there is a clear systematic excess of O VI over O V. We note, however, that the O V λ629.730 line becomes optically thick ($\tau = 1$) at an apparent column density of 1.2×10^{12} cm^{-2} (km s^{-1})$^{-1}$, whereas the O VI λ1031.927 line becomes optically thick at 2.8×10^{12} cm^{-2} (km s^{-1})$^{-1}$. So the differences in the profiles may be due to the effects of unresolved saturation.

We assume from the kinematic similarity of the O V and O VI apparent column density profiles that the two species arise in the same gas. With only two ions with broad kinematics, however, it is difficult to motivate a single ionization mechanism. Thus, we consider both collisional ionization equilibrium (CIE) and photoionization equilibrium (PIE) processes. In either case, the ionization level (determined by temperature in CIE, or by ionization parameter in PIE) and total oxygen column density can be gauged from the O VI/O V column density ratio. Inspection of the integrated column densities in Table 3 reveals that the O VI/O V ratio is slightly higher on the blue wing than the red wing, implying slightly higher ionization, although in both cases the ratio is nearly unity. In CIE, this is easily achieved at a temperature of $\log T(\mathrm{K}) \sim 5.5$. Photoionization by the quasar can also produce such a ratio with an ionization parameter of $\log U \sim -0.9$. We note that, in either case, thermal broadening produces a line width that is smaller than observed [$b_{\mathrm{thermal}}(\mathrm{O}) \lesssim 18$ km s^{-1} vs. $b \sim 23-40$ km s^{-1}], so there are likely other contributions to the kinematics.

In Figure 13 we compare the predicted N IV, O IV, and Ne VIII apparent column density profiles from CIE and PIE models with the observed profiles. These profiles were generated by first assessing the temperature profile (for CIE) or ionization parameter profile (for PIE) that reproduces the O VI/O V ratio at each velocity bin. The apparent column density profiles were computed from the ionization fractions implied by the temperature/ionization parameter profiles and assumed solar relative abundances from Asplund et al. (2004) N/O = 0.132, Ne/O = 0.151:

$$N(\mathrm{X}, i) = N(\mathrm{O}, 5)\left[\frac{f(\mathrm{X}, i)}{f(\mathrm{O}, 5)}\right]\left(\frac{\mathrm{X}}{\mathrm{O}}\right), \quad (9)$$

where $N(\mathrm{X}, i)$ is the column density (or apparent column density per unit velocity) of the ith ionization stage of element X, $f(\mathrm{X}, i)$ is the ionization fraction of that ion, and (X/O) is the abundance of X relative to oxygen. (This is a more general recasting of eq. [8].) All quantities are taken to be functions of velocity. As mentioned above, the ionization fractions are determined by temperature in CIE models, or by ionization parameter in PIE models. The temperature profile was computed using the CIE tables from Sutherland & Dopita (1993). The ionization parameter profile was computed using a grid of CLOUDY models assuming the quasar radiation field. In both ionization scenarios, detectable (and similar) amounts of O IV are produced, although not enough to fully explain the observed profile. Under the assumption of solar relative abundances, the CIE model does not produce N IV (at the requisite temperature to satisfy the O VI/O V ratio), while the PIE model produces small amounts. At least some of the O IV and N IV must reside in a separate phase of gas.

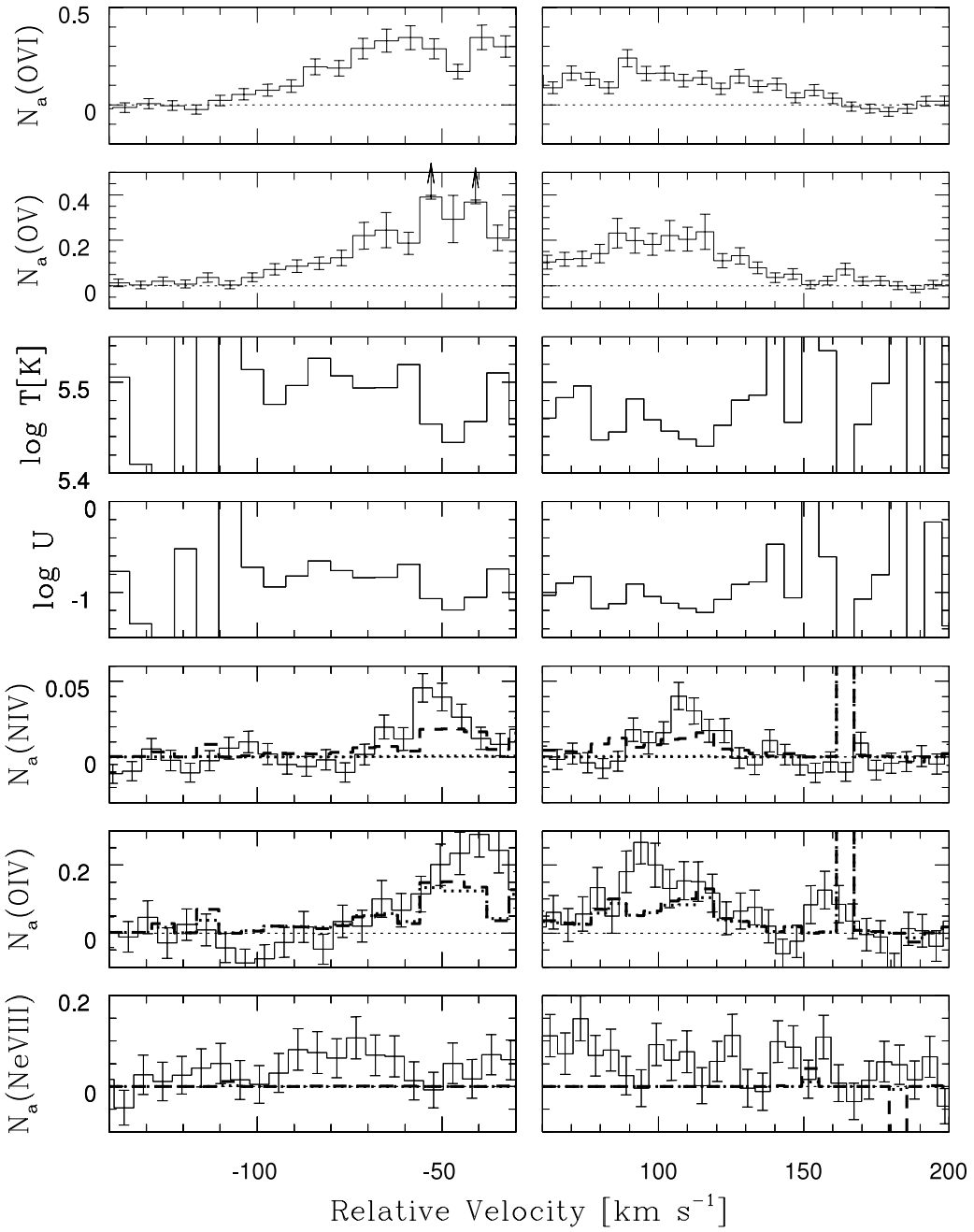

FIG. 13.—Predictions from CIE and PIE models on the apparent column density profiles of N IV, O IV, and Ne VIII, where the ionization level is tuned to match the O V–VI profiles. On the left we show the analysis of the broad component on the blue wing of the absorption-line system. On the right, we show the same for the component on the red wing. The top two panels on each side show the O VI, and O V apparent column density profiles. [Units on all apparent column density profiles are 10^{13} cm^{-2} (km s^{-1})$^{-1}$.] The next two panels show to the optimal temperature (for CIE) and ionization parameter (for PIE) as a function of velocity that reproduces the O VI/O V column density ratio. In the bottom three panels, we show the observed apparent column density profiles of N IV, O IV, and Ne VIII (*solid histogram with error bars*), and the predicted profiles from CIE (*dotted histogram*) and PIE (*dashed histogram*) models and assuming solar relative abundances (N/O = 0.132, Ne/O = 0.151). [*See the electronic edition of the Journal for a color version of this figure.*]

It is noteworthy that neither model of the O V– and VI–bearing gas is able to produce any Ne VIII (under the assumption of solar relative abundances), as shown in the bottom panel of Figure 13. This may be an indication (in addition to the lack of kinematic similarities) that Ne VIII is produced in a completely separate, very highly ionized phase of gas. Such a phase would probably have a temperature of $\log T(\mathrm{K}) \sim 5.85$, if collisionally ionized, or $\log U \sim +0.4$, if photoionized. At these ionization levels, all the oxygen would be in the form of O VII. Assuming the solar relative abundance, we predict column densities in the range $\log N(\mathrm{O\ VII})(\mathrm{cm}^{-2}) = 15-15.5$ for each of the two wings. If the metallicity of this very highly ionized phase is solar, then the total hydrogen column density for each wing is $\log N(\mathrm{H})(\mathrm{cm}^{-2}) = 18.3-18.8$. However, the origin of this gas, and therefore its metallicity, is unclear. It could arise near the quasar, or far from it in the halo of the host galaxy.

An alternative to a separate phase of gas that could potentially explain the observed column densities/profiles of this wide range is nonequilibrium processes. For example, from an apparent correlation between N(O VI) and b(O VI) Heckman et al. (2002) propose that O VI arises in postshocked, radiatively cooling gas. Using cooling functions from Sutherland & Dopita (1993), they

TABLE 4
Comparison of High-Ionization Species with Nonequilibrium Models

Component/Model	N(Ne VIII)/N(O VI)	N(O V)/N(O VI)
$-140 \leq v$(km s^{-1}) ≤ -30	0.23 ± 0.06	0.83 ± 0.12
$+60 \leq v$(km s^{-1}) $\leq +200$	0.58 ± 0.11	1.17 ± 0.13
Isobaric cooling[a]	1.26	0.5
Isochoric cooling[a]	0.5	0.6
Shock ionization[b]	0.005–1.026	0.097–0.433

Note.—Errors on all quantities are quoted at 1 σ confidence.

[a] From Heckman et al. (2002), these ratios are based on radiative cooling models from Sutherland & Dopita (1993), assuming a shock velocity of 600 km s^{-1}, a postshock velocity of 100 km s^{-1}, and an initial temperature of 10^6 K.

[b] From Dopita & Sutherland(1996); these ratios assume shock velocities in the range 100-500 km s^{-1} and magnetic parameters in the range 0–4 μG cm$^{3/2}$.

predict column densities of other ions that exist in both hotter gas (like that producing Ne VIII) that would exist prior to O VI, and cooler gas (like that producing O V) that exists after. In Table 4 we report the observed Ne VIII/O VI, and O V/O VI column density ratio for the broad components on the blue and red wings. In addition, we report the predicted column density ratios from Heckman et al. (2002) for gas behind a 600 km s^{-1} shock cooling from $T = 10^6$ K and a postshock velocity of 100 km s^{-1} in two extremes, isobaric and isochoric cooling. From the table, only the Ne VIII/O VI column density ratio on the red wing could be explained through a radiative cooling scenario somewhere between these two extremes. However, in both components, the observed O V/O VI ratio is too large for either extreme; there is too much O V (relative to O VI) in the observed profile.

Another alternative nonequilibrium process is photoionization by a local radiation field produced by a fast, highly radiative, magnetic-pressure–supported shock. Dopita & Sutherland (1996) present such a scenario and provide tables of predicted column densities of a multitude of ions for a range of shock velocities (200–500 km s^{-1}) and magnetic parameters, $B/n^{1/2}$ (0–4 μG cm$^{3/2}$). The range of Ne VIII/O VI and O V/O VI ratios predicted by these models is also listed in Table 4. In this case, the Ne VIII/O VI ratio of both components could be explained under this scenario. However, as with the radiative cooling scenario, the predicted O V column relative to O VI is much smaller (by about a factor of 2) than observed. Other nonequilibrium scenarios include turbulent mixing of entrained gas (e.g., Slavin et al. 1993), and magnetic conduction through the interface between gases (e.g., Borkowski et al. 1990). However, these papers make predictions on the column density of more commonly detected ions, such as C IV, N V, and Si IV which are not covered by our data. Thus we cannot address the applicability/validity of these scenarios to the gas in the broad components.

5. DISCUSSION

We have analyzed the detailed ionization and geometric constraints and physical conditions provided by the wide range of ionization species detected in the absorption-line system associated with the quasar HE 0226−4110. The rest-frame wavelength coverage of our *FUSE* and *HST* STIS data, 610–1150 Å, provide coverage of six ionization stages of oxygen. Four stages are detected (O III–VI) and these show a remarkable ionization-dependent complexity in the gas kinematics. Comparatively low-ionization species like H I, C III, and O III are only detected in a single narrow component. Two broad components flank this component in velocity and appear mostly in high-ionization species. Intermediate-ionization stages, like N IV and O IV, are featured in both a narrow component (although with in a separate phase that is offset in velocity) and the two flanking broad components. An additional narrow component exists in this associated system that is only apparently detected in O VI. In the following sections we discuss possible origins, locations, and structural geometries for these components. (As has been our convention throughout this paper, we quote velocities relative to $z_{\rm abs} = 0.4925$.)

5.1. *Low- and Moderate-Ionization Gas at* $v = -8$ km s^{-1} (*in the* $z_{\rm abs} = 0.4925$ *Rest Frame*)

The narrow low and moderate-ionization component detected in H I, C III, and O III is the most well-constrained component in this absorption-line system. All three species appear to arise in the same phase of gas, as motivated by the kinematics of profiles. Using measurements of the H I/O III and C III/O III ratios (and limits on the O IV/O III and N IV/O III ratios), we determine the optimal metallicity, ionization parameter and total hydrogen column density of the O III–bearing gas (see eq. [4]). We now focus on the implications of these results on the location and geometry of the gas.

The ionization parameter is related to the spectral energy distribution of the quasar (L_ν), the distance between the absorber and the quasar central engine (r), and the density of the absorber (n) via

$$U = \frac{1}{4\pi r^2 nc} \int_{\nu_{\rm LL}}^{\infty} \frac{L_\nu}{h\nu}\, d\nu, \tag{10}$$

where $\nu_{\rm LL}$ is the frequency of the Lyman limit. For the spectral energy distribution specified in the photoionization models, this relationship reduces to

$$\begin{aligned} \log U &= -1.43 - \log n_{3.5} - 2 \log r_{21.5}, \\ n_{3.5} &= n/(10^{3.5}\ {\rm cm}^{-3}), \\ r_{21.5} &= r/(10^{21.5}\ {\rm cm}) = r/(1\ {\rm kpc}). \end{aligned} \tag{11}$$

The reference values for the density and distance are taken from current limits for intrinsic narrow absorption lines based on variability analyses (e.g., Wise et al. 2004; Narayanan et al. 2004; Ganguly et al. 2001b; Hamann et al. 1997a).

Likewise, the thickness scale of the absorbing gas is given by the ratio between the total hydrogen column density and the density of the gas. Combining equations (4) and (11), we find the following relationships for the location (r) and thickness (Δr) of the absorbing gas:

$$\begin{aligned} r &= 1.5 n_{3.5}^{-1/2}\ {\rm kpc}, \\ \Delta r &= 7.3 n_{3.5}^{-1}\ {\rm AU}. \end{aligned} \tag{12}$$

Before considering possible locations for the gas and related implications, we make one observation regarding the spatial extent (i.e., perpendicular to the line of sight) of the absorbing structure. Given that the absorber fully occults the UV continuum as evidenced by the zero flux levels of the C III λ977.020 and H I Lyβ lines, we can place a lower limit on extent of the absorber on the plane of the sky. Using our fit to the optical spectrum (in particular, our characterization of the Hβ emission line and the underlying power law continuum), we estimate that the black hole powering the quasar has a mass of $10^{8.7}$–$10^{9.6}\ M_\odot$. The range comes from using the scaling relations of Kaspi et al. (2000) and Peterson et al. (2004). Black holes with masses in that range have a gravitational radius of $r_g = 4.6$−38 AU. The UV

continuum is typically emitted in the region between $6r_g$ and $60r_g$ (e.g., Murray et al. 1995), with the bounds arising from the radius of last stable orbit (for a nonrotating black hole) and the radius at which the accretion-disk becomes optically thick. Thus the absolute minimum spatial extent of the cloud is $w \approx 600$ AU ($2 \times 60r_g$). Combining this with equation (12) The aspect ratio of the O III–bearing gas (width/thickness) is then

$$w/\Delta r \gtrsim 82 n_{3.5},$$
$$w/\Delta r \gtrsim 82\left(\frac{r}{1.5\ \mathrm{kpc}}\right)^{-2}. \quad (13)$$

In the second expression, we have used the relationship between the source-absorber distance, and the absorber density.

From a consideration of the statistical frequency of high-ionization (C IV, N IV, and O VI) associated absorbers in low-redshift ($z \lesssim 1$) quasars as a function of quasar redshift, Ganguly et al. (2001a) placed high-ionization AAL gas in the shearing region between the outflowing from the accretion disk, and a low-density, very highly ionized medium above the wind (see their Fig. 13). This scenario was physically motivated by the hydrodynamic simulations of Proga et al. (2000), which show instabilities in that region. For the O III–bearing gas to reside in that region (within a parsec of the UV continuum source), the gas must have a density in excess of 7×10^9 cm^{-2}, and an aspect ratio larger than 1.8×10^8. While the density is fairly reminiscent of the broad-line regions of quasars, the aspect ratio is unphysically large. Similarly, the placement of intrinsic narrow absorption lines by Elvis (2000) at the bottom of the outflow would require even larger densities and aspect ratios. This does not necessarily rule out either model, since those models only apply to high-ionization absorbers. Rather, this AAL, and in particular the O III–bearing gas, points to an incompleteness in the models purporting to place gas that is related (at least statistically) to quasars. In the following subsections, we entertain two possible, alternative locations for the gas producing the O III–bearing gas, the narrow emission line region of the quasar, and the halo of the quasar host galaxy.

5.1.1. *Narrow Emission Line Gas?*

In principle, combining information from [O III] λ5007 emission and O III λ832.927 absorption, we can potentially constrain the density (n) of the absorbing gas. Density information is important since it enables an assessment of the geometry of the absorbing material courtesy of equation (9). In some associated absorbers, density constraints (e.g., from excited fine-structure lines) combined with photoionization models have indicated large distances between the associated absorber and the QSO central engine (e.g., Morris et al. 1986; Tripp et al. 1996; Hamann et al. 2001; Eracleous et al. 2003; Gabel et al. 2004). In other cases, similar analyses place the AALs close to the central engine (e.g., Srianand & Petitjean 2000). The density estimates on these rely on excited states of comparatively low-ionization species, namely, C II*, Si II*, Fe II*, and C III* that are not widely detected in AALs, so it is not clear how broadly applicable the results of those studies are in understanding the distribution of location of AAL gas. The potential association of O III absorption in the narrow emission line region, then, has paramount importance to this issue, since strong narrow emission lines are far more common in AGNs.

In trying to associate this absorption-line gas with the narrow emission line gas observed in [O III] λ5007, it is important to consider the geometry and kinematics of the emitting region compared to the pencil-beam probe producing the absorption. We

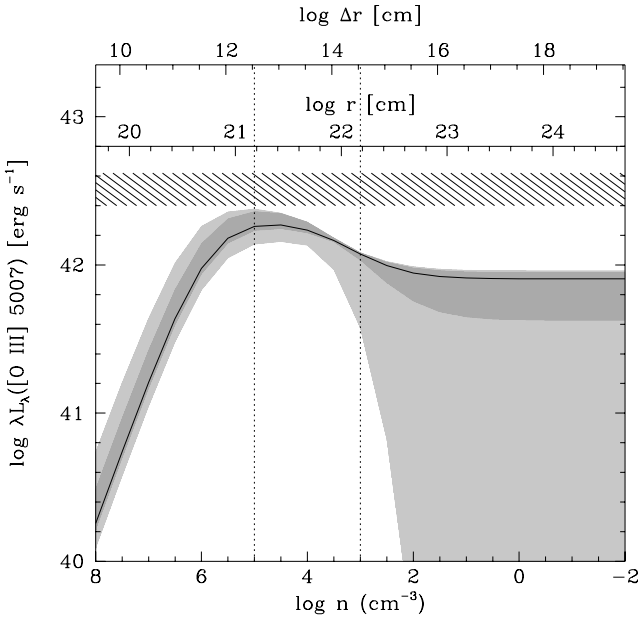

FIG. 14.—Plot shows the predicted [O III] λ5007 line luminosity as a function of gas density. The solid curve shows the grid of CLOUDY models using $\log U = -2.29$, and $[\mathrm{O/H}] = +0.12$. The shaded regions around the solid curve represent the set of models allowed by the 1 and 2 σ uncertainties in the ionization parameter and metallicity from the absorption-line diagnostics (see Figs. 7 and 8). The hatched region at $\log \lambda L_\lambda$([O III] λ5007)(ergs s^{-1}) = 42.4−42.62 marks the 1 σ confidence luminosity of the EM6 emission-line component, which we associate with this gas. The dashed vertical lines at $\log n(\mathrm{cm}^{-3}) = 3$ and 5 indicate the typical range of densities expected for the narrow emission line region gas using emission-line diagnostics. The top two axes indicate the inferred absorber thickness [Δr, assuming a total hydrogen column density $\log N(\mathrm{H})(\mathrm{cm}^{-2}) = 17.54$] and distance from the accretion disk (r). These axes are implicitly dependent on the ionization parameter, and therefore only apply to the solid curve. [*See the electronic edition of the Journal for a color version of this figure.*]

note a few basic facts (in addition to those mentioned above regarding physical conditions and geometry) that a narrow emission line region model incorporating the O III-absorbing gas should address: (1) a match in velocity [z_{em}([O III]) = 0.4928 ± 0.0001, z_{abs}(O III) = 0.49246 ± 0.00006, $\Delta v = 68 \pm 23$ km s^{-1}; see Table 1 and § 4] between the absorption- and emission-line centroid; (2) a factor of 32 difference in the velocity widths (FWHM ∼ 470 km s^{-1} for emission, FWHM∼15 km s^{-1} for absorption); and (3) an [O III] λ5007 luminosity of 3.2×10^{42} ergs s^{-1}.

We first consider whether gas with $\log U = -2.29$ and $[\mathrm{O/H}] = +0.12$ (as implied by the analysis of the absorption lines) can reproduce the observed luminosity. To do so, we ran another grid of CLOUDY models over density, placing the gas at a distance that reproduces an ionization parameter of $\log U = -2.29$. At each grid point, we compute the [O III] λ5007 line luminosity and compare that to the observed line luminosity for emission-line component 6 from our fit to the [O III] λ5007 line in § 3 (see Table 1), since this is the component whose redshift matches that of the O III λ832.927 absorption. In these models, the gas is assumed to exist in the thin spherical shell that surrounds the pointlike central engine. The absorption arises from the pencil-beam probe through the shell toward the observer, while the emission arises (isotropically) from the integration over the entire shell.

The results of the grid of CLOUDY models are shown in Figure 14. On the top axes of the plot, we show the implied distance, $\log r[\mathrm{cm}] = 21.5 + 0.5(4.36 - \log n[\mathrm{cm}^{-3}])$, and thickness, $\log \Delta r(\mathrm{cm}) = 17.54 - \log n(\mathrm{cm}^{-3})$. The model curve shows a power-law decrease of the [O III] λ5007 line luminosity with

increasing density starting at $\log n(\mathrm{cm}^{-3}) \sim 5$. At smaller densities, the curve falls off and flattens to a constant line luminosity whose value depends on the ionization parameter and metallicity. The shaded regions around the plotted curved represent families of models that lie in the 1 and 2 σ confidence regions shown in Figure 8. Models with higher ionization parameters and/or metallicities decrease the constant luminosity to which the curve levels out. The hatched region across the top of the figure is vertically placed at the observed luminosity of the EM6 component, with the thickness of the region representing the 1 σ confidence interval. The vertical dotted lines are placed to indicate the range of densities, $\log n[\mathrm{cm}^{-3}] = 3-5$, commonly associated with narrow emission line region gas. The plot shows that there is no density at which the model predicts sufficient line luminosity to match the observation, although at the $\sim$1.5 σ level, there is reasonable agreement around $n \sim 10^5$ cm^{-3}.

In principle, the discrepancy could be further explained by the fragmentation of the shell into several smaller clouds within the narrow emission line region (with only one cloud producing the absorption) or with the inclusion of other important physical processes (such as shocks). Such an explanation may be required in order to reconcile the model with the observed velocity width of the EM6 component ($\sim$470 km s^{-1}). A static thin shell with an internal velocity dispersion of $\sim$15 km s^{-1} (as indicated by the pencil-beam absorption-line probe) does not yield an overall velocity width of 470 km s^{-1} from the emission-line gas. (In order to explain the 68 km s^{-1} blueshift of the absorption line relative to the emission line, one might invoke an expanding thin shell, but even such a shell would not produce the observed emission-line velocity width.) With a fragmented shell, a possible solution is that the bulk velocity dispersion of the resulting clouds (arising perhaps from orbital motion about the central black hole) is several hundred km s^{-1}, while the internal velocity dispersion of any single cloud is as indicated by the absorption-line profiles. This scenario has two advantages over a simple thin shell model: (1) a thin shell may have stability problems, and (2) the added surface area from fragmentation could yield the factor of 2 difference between the predicted and observed [O III] λ5007 luminosities.

However, there are other potential self-consistency problems with the absorbing gas with a density of $n \sim 10^5$ cm^{-3}. The implied distance between the absorber and the accretion disk is $r \approx 0.5 n_5^{-1/2}$ kpc. While this is reasonable for a location within the narrow emission line region (e.g., Schmitt et al. 2003; Bennert et al. 2002), the implied cloud thickness is extremely small, $\Delta r \approx 0.24 n_5^{-1}$ AU, implying a minimum aspect ratio (see eq. [13]) of $\approx 1200 n_5$ for the cloud. For the model to provide a self-consistent representation of data, the gas probed by the absorption must be distributed in the form of a sheet or a closed spherical shell (or sets of sheets/shells), rather than a discrete almost-spherical cloud. Possibly, such a deformation might result from the hydrodynamics of gas orbiting a central supermassive black hole, although such a deformed cloud would probably fragment further. Another potential problem with this scenario is that only one cloud is seen in absorption. While it is possible that only one cloud would be intercepted by the sight line in this patchy cloud scenario, it is improbable. Only future observations to look for variability in the O III absorption profile and/or higher resolution observations (spatial and spectral) of the [O III] λ5007 can address the patchiness of the narrow emission line region and the number of clouds intercepted by the absorption-line probe.

A number of additional observational tests are required to fully explore the implications of this result. Additional data covering the O III λ832.927 line in the associated absorption of other quasars is required to ascertain the frequency in which gas in the narrow emission line region is observed in absorption and the fraction of associated absorbers that originate in this region. Since this associated absorber clearly has many components with different gas phases, it is likely that several different regions contribute to the observed profiles. Spectra with high-resolution ($\lambda/\Delta\lambda \geq 10^4$) are required to disentangle the relative importance of the different quasar emitting regions to the observed frequency of associated absorbers. For this and other quasars whose spectra feature associated absorption in O III λ832.927), higher resolution spectroscopy of the [O III] λ5007 line would be useful in directly, and more precisely, comparing the kinematics of the extended narrow emission-line region with the pencil-beam probe provided by the O III absorption. The density diagnostics available from the analysis of emission lines would greatly assist in disentangling the geometry of intrinsic absorbers.

5.1.2. *Quasar Host Galaxy Halo Gas?*

Another potential location for the O III–absorbing gas is the halo of the quasar host galaxy. If the gas were located, for example, 10 kpc away from the central engine, then (by eq. [12]) the density of the gas would be $\sim$230 cm^{-3}, and the thickness of the gas would be $\sim$100 AU. The resulting aspect ratio (by eq. [13]) would be >6, so such a structure would still be rather nonspherical. Are there local analogs of such a structure? High-velocity clouds such as Complex C or the Magellanic Stream may have such aspect ratios, but do not have such large densities (e.g., Sembach et al. 2001; Wakker 2001, 2004; Tripp et al. 2003; Fox et al. 2004). If the gas were $\gtrsim$13.5 kpc away from the central engine, also within the halo of the quasar host galaxy, that would allow for a spherical structure with an absorbing thickness scale >600 AU. At such a distance, the density is smaller than 37 cm^{-3}. However, clouds in the halo (or outer corona) of the Galaxy do not have the high (supersolar) metallicity (e.g., Wakker 2001, 2004; Richter et al. 2001; Tripp et al. 2003) observed in the O III–absorbing gas.

While there are no local analogs of an absorbing structure that exists in the halo with supersolar metallicites and a large density, such an idea is not without precedent. The associated absorber observed toward 3C 191 (Hamann et al. 2001) features very similar properties—gas with a density of $\sim$300 cm^{-3}, residing 28 kpc from the quasar central engine. However, that absorber is detected in very low ionization gas (Mg II, C II, Si II) and excited state lines from C II* and Si II*, which are not present in the O III–absorbing gas in this associated absorber. Moreover, the low-ionization lines observed in the 3C 191 associated absorber exhibit the signature of partial coverage (dilution of the absorption-line troughs unocculted light) and the coverage fractions imply gas clouds with a spatial extent smaller than 0.01 pc. (The thickness of the 3C 191 associated absorber is unknown as Hamann et al. 2001 are only able to place upper limits on the total hydrogen column density.) In addition, the 3C 191 associated absorber is apparently outflowing (it is blueshifted by more than 400 km s^{-1} relative to the broad emission lines), whereas the O III–absorbing gas in this associated absorber is at a velocity fairly coincident with the [O III] λ5007 narrow emission line. It is possible that O III gas in this associated absorber is a slightly higher ionization analog of that absorber. If so, then the speculation by Hamann et al. 2001 that the gas may be residue from a nuclear starburst superwind may be applicable. It is unlikely that this material is the result of an ejection from a BAL wind as the gas appears to be at rest (or close to it) with respect to the narrow emission region, which would imply a severe deceleration (by several orders of magnitude).

5.2. *Moderate- and High-Ionization Gas at $v = 0$ and $+50$ km s^{-1} (in the $z_{abs} = 0.4925$ Rest Frame)*

Additional narrow features are detected in this associated absorption-line system, but the physical conditions of the gas are much less constrained than the O III–bearing gas. Both of these components have a higher ionization than the other narrow component. The $v = 0$ km s^{-1} component is detected as a single narrow feature in intermediate-ionization species such as N IV, O IV, and S IV, while the $v = +50$ km s^{-1} component is detected as a narrow feature in O VI only. Absorption from other intermediate- and high-ionization species—O V and Ne VIII—is evident, but kinematics of these species do not trace the narrow components. There is no detectable H I that is associated with either of these components, as all the observed H I appears over velocity range and has the kinematic appearance of the O III–bearing gas. Whether there is a relationship between these components either to each other, or to the O III–bearing gas is unclear. The gas could lie close to the quasar central engine, or far out in a companion galaxy.

The velocity widths of these two components are fairly narrow [$b(v = 0$ km s$^{-1}) \sim 15$ km s^{-1}, $b(v = +50$ km s$^{-1}) \sim 9$ km s^{-1}][8] and, in the case of the $v = +50$ km s^{-1} component, suggest that collisional processes are not important in the ionization, leaving radiative processes as the likely dominant source of ionization. Even if the gas producing these components were far from the central engine, perhaps in a dwarf companion to the quasar host galaxy, photoionization by the central engine is likely the dominant source of ionizing photons. For the $v = +50$ km s^{-1} narrow component, we used the available constraints from O V and Ne VIII to infer that the gas must have an ionization parameter in the range $-0.35 \lesssim \log U \lesssim -0.02$. However, since there is no information on the density of this component (e.g., via association with a line-emitting region, or excited state transitions, or time variability), it is difficult to know where the gas is located relative to quasar central engine (since the distance between the accretion disk and the absorber is degenerate with the density [$U \propto L/nr^2$]).

One possible interpretation is that these components arise in structures similar to that of the other narrow component, but with smaller densities (thus producing higher ionization species). For the narrow O VI component, if the gas lies within the narrow emission line region of the quasar, then it has a density in the range $10^{2.69} \lesssim n[\mathrm{cm}^{-3}] \lesssim 10^{3.02}$. This is consistent with the range of densities typically found in quasar narrow emission line regions. The gas producing the narrow O VI absorption would not contribute significantly to the formation of the narrow emission lines since the gas is too ionized. If the total hydrogen column density of the narrow O VI component is in the range $17.75 \lesssim \log N(\mathrm{H})[\mathrm{cm}^{-2}] \lesssim 18.1$ (as would be implied if the metallicity were similar to the O III component), then the thickness of the gas sheet producing the narrow O VI component lies in the range $35 \lesssim \Delta r[\mathrm{AU}] \lesssim 170$, and an aspect ratio of at least 3.5. Using the absolute maximum total hydrogen column density (as derived by the nondetection of H I and the limiting ionization fraction), the aspect ratio cannot be smaller than 1.4 (if the gas lies with the narrow emission line region).

Alternatively, if the narrow O VI gas is in the halo of the quasar host galaxy, 10 kpc away from the central engine, then it would have a density in the range $0.5 \lesssim n[\mathrm{cm}^{-3}] \lesssim 1.1$, which would be consistent with local versions of halo gas clouds. While these are only two of many possible scenarios for these higher ionization components, they have the attraction of readily explaining why all three narrow components arise within the same absorption-line system very close in velocity (within 50 km s^{-1}).

It is noteworthy that Bergeron et al. (2002) and Carswell et al. (2002) detect O VI components at $z_{abs} \gtrsim 2$ that are also narrow enough to imply photoionization. In particular, Bergeron et al. (2002) detect a component at $z_{abs} = 2.36385$ in the direction of Q0329-385 ($z_{em} = 2.423$) with a similar b-value as the $v = +50$ km s^{-1} component in this associated system. (The difference in redshift corresponds to a velocity separation of 5225 km s^{-1}, which is close to the arbitrary cutoff for associated absorption-line systems.) That component is detected in H I and has a N(O VI)/N(H I) ratio of $\approx$0.09. Our narrow O VI component is not detected in H I and has a ratio of N(O VI)/N(H I) $\gtrsim 5$. In fact, in all of the cases presented by both Bergeron et al. (2002) and Carswell et al. (2002), the narrow, hence photoionized, O VI is accompanied by detection of H I, in marked contrast to the $v = +50$ km s^{-1} component in this associated absorption-line system. (Carswell et al. [2002] note that in all cases that they present, the H I column density is larger than 2×10^{14} cm^{-2}. None of their components appear to have metallicities in excess of [C/H] ≈ -1.7.) Bergeron et al. (2002) report that their photoionized O VI components (with only one exception) have metallicities in range $-2.5 \leq$ [C/H] ≤ -0.5, with supersolar [O/C]. This is consistent with our constraint on [O/H] (≥ -0.62) for the $v = +50$ km s^{-1} component.

In many of the cases studied by Bergeron et al. (2002; including the one mentioned above), the narrow O VI components are accompanied by detections of C IV (and occasionally N V). For the narrow O VI component in this absorption-line system, the strong UV doublet from neither species is covered by our spectra. If the photoionization models described in § 4.1.3 are an accurate representation of the O VI–bearing gas, then we predict column densities in the range $12.21 \lesssim \log N(\mathrm{C\ IV}) \lesssim 12.4$, and $12.74 \lesssim \log N(\mathrm{N\ V}) \lesssim 12.82$ (for [O/C] = [O/N] = 0). For comparison, the associated component from the Bergeron et al. (2002) study mentioned above has $\log N(\mathrm{C\ IV}) = 12.33$, and $\log N(\mathrm{N\ V}) = 12.00$. The C IV column density is within the range predicted for the $v = +50$ km s^{-1} component (even if [O/C] were slightly supersolar), but the N V column density is smaller than that of the $v = +50$ km s^{-1} component (if N/O is solar). If the N/O abundance in the $v = +50$ km s^{-1} component is subsolar by 0.7 dex, then the two are components are very similar aside from the differences in redshift and H I column density. Bergeron et al. (2002) find precisely such an abundance requirement for their $z_{abs} = 2.25146$ component ([O/N] ≥ 0.7). If this is a general property, then the $v = +50$ km s^{-1} component in this associated absorption-line system is very consistent with the populations of photoionized O VI discussed by Bergeron et al. (2002) and may be higher metallicity analogs to those studied by Carswell et al. (2002).

5.3. *Broad Components*

Intermediate- and high-ionization species, namely, N IV, O V–VI, and Ne VIII, show absorption in two relatively broad components. In O VI, the absorption in these two components constitutes roughly 30% of the total integrated column density. The kinematics of O V and O VI appear to trace each other, suggesting that the two arise in the same phase of gas. Moreover, there is no evidence for trough-dilution by unocculted quasar light, so it is unlikely that these components arise from the quasar outflow (depending on the orientation of the accretion disk and possible presence of a scattering medium).

Since many different physical process could be involved in the production of this gas (photoionization by the quasar central engine, collisional ionization from shocks, etc.), it is unclear what

[8] Both of these values were obtained from direction integration of the second moment of the apparent optical depth profile.

ionization model to apply in order to infer physical conditions. In § 4.2 we explored various ionization models—CIE, PIE, radiative cooling (RC) as described by Heckman et al. (2002), and shock ionization (SI) as described by Dopita & Sutherland (1996). CIE and PIE models that are tuned (through the temperature or ionization parameter) to reproduce the observe O v and O vi column densities are unable to fully explain the presence of N iv, O iv, and Ne viii in the same phase of gas (Fig. 13). The RC and SI models are unable to even simultaneously reproduce the O v and O vi column densities under the range of parameters considered (see Table 4).

Of the models considered, photoionization by the quasar is able to explain the largest number of species simultaneously. However, such a model requires additional phases to explain the presence of Ne viii, and some of the N iv and O iv (and it is not clear what ionization models are appropriate for such phases). For the phase producing O v–vi, if photoionization by the quasar is the correct model, then O vii should be the dominant ionization stage in these components. An X-ray spectrum (e.g., with *Chandra* or *XMM-Newton*) to look for O vii absorption would help to elucidate the important physical processes producing the broad components. Although the total column density of O vii predicted by these components ($N \lesssim 10^{15}$ cm^{-2}) would probably not be detectable, the higher ionization gas producing the Ne viii may be detectable. Information on the higher ionization stages of oxygen would compete the picture of the ionization structure of gas in this absorption-line system.

Like the narrow higher ionization components, there is no density information in the broad components. Thus, it is not possible to transform the optimal ionization parameter into a distance. Likewise, there is no metallicity information, so it is not possible to robustly gauge the thickness of the absorbing regions. There are several plausible locations for this gas (ablation off an obscuring torus, a diffuse medium cospatial with the narrow emission-line region, satellite dwarf galaxies, etc.) and we cannot distinguish between them.

6. SUMMARY OF RESULTS

We have obtained high-resolution, rest-frame extreme ultraviolet spectra of the quasar HE 0226−4110. The spectra cover the wavelength range 610–1150 Å in the rest-frame of the quasar. We detect an associated absorption-line system in a wide range of ionization species, including several Lyman series lines, Ne viii, and four adjacent stages of oxygen, O iii–vi. Strong transitions from O i and O ii are also covered by our data, but are not detected. The high quality of these spectra allow us to study the kinematic structure of the gas. A summary of our results follows.

1. The O iii λ832.927 line is detected in a single narrow component at $v = -8$ km s^{-1} in the $z = 0.4925$ reference frame. The kinematics of the absorber indicate that all the detected H i and C iii are associated with this component, and we use the O iii profile to gauge the column density ratios of the narrow emission line region gas. Using CLOUDY photoionization models to constrain physical parameters, we find that this cloud has a metallicity of $[\mathrm{O/H}] = +0.12^{+0.16}_{-0.03}$, an ionization parameter $\log U = -2.29^{+0.02}_{-0.23}$, and a total hydrogen column density of $\log N(\mathrm{H}) = 17.54^{+0.04}_{-0.25}$.

2. We detect additional narrow components at 8 and 58 km s^{-1} redward of the O iii–bearing gas (at $v = 0$ and +50 km s^{-1} in the $z = 0.4925$ rest-frame, respectively). These components are detected in higher ionization species. The $v = 0$ km s^{-1} component is detected as a single narrow feature in N iv, O iv, and S iv, while the $v = +50$ km s^{-1} component is similarly detected only in O vi. Absorption from O v and Ne viii is detected at the same velocities, but the kinematics rule out a direct association. The O vi profile is too narrow to be produced by collisional processes. Using limits on the Ne viii/O vi and O v/O vi column density ratios, we constrain the ionization parameter of the $v = +50$ km s^{-1} component to the range $-0.35 \lesssim \log U \lesssim -0.02$.

3. Two broad, smooth components are also detected in N iv, O v–vi, and Ne viii. We find no evidence for the dilution of troughs expected from gas arising in an accretion-disk outflow. There is insufficient information to propose a unique ionization scenario (both collisions and photons could contribute to the ionization). Radiative cooling and shock ionization models are unable to produce sufficient amounts of O v in the ranges of model parameters considered by Heckman et al. (2002) and Dopita & Sutherland (1996) to match the observed column density. Photoionization by the quasar is able to explain some N iv and O iv in a phase tuned to produce O v–vi. However, other phases are required to fully explain the observed profiles. A separate phase is required, regardless of mechanism, to explain the presence of Ne viii.

The STIS observations of HE0226−4110 were obtained under the auspices of *HST* program 9184, with financial support through NASA grant HST-GO-9184.08-A from the Space Telescope Science Institute. T. M. T. was also supported in part by NASA grant NNG 04GG73G. R. G. is grateful to Toru Misawa and Chien Yi Peng for helpful discussions. The authors also thank the anonymous referee for a thorough review, which resulted in a more streamlined presentation.

REFERENCES

Arav, N., Korista, K. T., & de Kool, M. 2002, ApJ, 566, 699
Arav, N., Korista, K. T., de Kool, M., Junkkarinen, V. T., & Begelman, M. C. 1999, ApJ, 516, 27
Asplund, M., Grevesse, N., & Sauval, A. J. 2005, in ASP Conf. Ser. 336, Cosmic Abundances as Records of Stellar Evolution and Nucleosynthesis, ed. F. N. Bash & T. G. Barnes (San Francisco: ASP), 25
Asplund, M., Grevesse, N., Sauval, A. J., Allende Prieto, C., & Kiselman, D. 2004, A&A, 417, 751
Baker, J. C., Hunstead, R. W., Athreya, R. M., Barthel, P. D., de Silva, E., Lehnert, M. D., & Saunders, R. D. E. 2002, ApJ, 568, 592
Barlow, T. A., & Sargent, W. L. W. 1997, AJ, 113, 136
Becker, R. H., White, R. L., Gregg, M. D., Brotherton, M. S., Laurent-Muehleisen, S. A., & Arav, N. 2000, ApJ, 538, 72
Becker, R. H., White, R. L., & Helfand, D. J. 1995, ApJ, 450, 559
Bennert, N., Falcke, H., Schulz, H., Wilson, A. S., & Wills, B. J. 2002, ApJ, 574, L105
Bergeron, J., Aracil, B., Petitjean, P., & Pichon, C. 2002, A&A, 396, L11
Borkowski, K. J., Balbus, S. A., & Fristrom, C. C. 1990, ApJ, 355, 501
Boroson, T. A., & Green, R. F. 1992, ApJS, 80, 109
Boyle, B. J., Shanks, T., Croom, S. M., Smith, R. J., Miller, L., Loaring, N., & Heymans, C. 2000, MNRAS, 317, 1014
Brandt, W. N., Laor, A., & Wills, B. J. 2000, ApJ, 528, 637
Brotherton, M. S., van Breugel, W., Smith, R. J., Boyle, B. J., Shanks, T., Croom, S. M., Miller, L., & Becker, R. H. 1998, ApJ, 505, L7
Carswell, B., Schaye, J., & Kim, T.-S. 2002, ApJ, 578, 43
Collins, J. A., Shull, J. M., & Giroux, M. L. 2005, ApJ, 623, 196
Crenshaw, D. M., et al. 2003, ApJ, 594, 116
Dopita, M. A., & Sutherland, R. S. 1996, ApJS, 102, 161
Elvis, M. 2000, ApJ, 545, 63
Eracleous, M., & Halpern, J. P. 2004, ApJS, 150, 181
Eracleous, M., Halpern, J. P., & Charlton, J. C. 2003, ApJ, 582, 633
Ferland, G. J., Korista, K. T., Verner, D. A., Ferguson, J. W., Kingdon, J. B., & Verner, E. M. 1998, PASP, 110, 761
Ferrarese, L., & Merritt, D. 2000, ApJ, 539, L9

Foltz, C. B., Chaffee, F. H., Weymann, R. J., & Anderson, S. F. 1988, in QSO Absorption Lines: Probing the Universe, ed. J. C. Blades, D. A. Turnshek, & C. A. Norman (Cambridge: Cambridge Univ. Press), 53
Foltz, C. B., Weymann, R. J., Peterson, B. M., Sun, L., Malkan, M. A., & Chaffee, F. H. 1986, ApJ, 307, 504
Fox, A. J., Savage, B. D., Wakker, B. P., Richter, P., Sembach, K. R., & Tripp, T. M. 2004, ApJ, 602, 738
Fox, A. J., Wakker, B. P., Savage, B. D., Tripp, T. M., Sembach, K. R., & Bland-Hawthorn, J. 2005, ApJ, 630, 332
Gabel, J., Kraemer, S., & Crenshaw, D. 2004, in ASP Conf. Ser. 311, AGN Physics with the Sloan Digital Sky Survey, ed. G. T. Richards & P. B. Hall (San Francisco: ASP), 239
Gabel, J. R., et al. 2003a, ApJ, 595, 120
———. 2003b, ApJ, 583, 178
Ganguly, R., Bond, N. A., Charlton, J. C., Eracleous, M., Brandt, W. N., & Churchill, C. W. 2001a, ApJ, 549, 133
Ganguly, R., Charlton, J. C., & Eracleous, M. 2001b, ApJ, 556, L7
Ganguly, R., Eracleous, M., Charlton, J. C., & Churchill, C. W. 1999, AJ, 117, 2594
Ganguly, R., Masiero, J., Charlton, J. C., & Sembach, K. R. 2003, ApJ, 598, 922
Ganguly, R., Sembach, K. R., Tripp, T. M., & Savage, B. D. 2005, ApJS, 157, 251
Gebhardt, K., et al. 2000, ApJ, 539, L13
Greenstein, J. L., & Schmidt, M. 1964, ApJ, 140, 1
Griffith, M. R., & Wright, A. E. 1993, AJ, 105, 1666
Grupe, D., Beuermann, K., Mannheim, K., & Thomas, H.-C. 1999, A&A, 350, 805
Grupe, D., Beuermann, K., Thomas, H.-C., Mannheim, K., & Fink, H. H. 1998, A&A, 330, 25
Hamann, F., Barlow, T. A., Beaver, E. A., Burbidge, E. M., Cohen, R. D., Junkkarinen, V., & Lyons, R. 1995, ApJ, 443, 606
Hamann, F., Barlow, T. A., & Junkkarinen, V. 1997a, ApJ, 478, 87
Hamann, F., Barlow, T. A., Junkkarinen, V., & Burbidge, E. M. 1997b, ApJ, 478, 80
Hamann, F., & Ferland, G. 1999, ARA&A, 37, 487
Hamann, F. W., Barlow, T. A., Chaffee, F. C., Foltz, C. B., & Weymann, R. J. 2001, ApJ, 550, 142
Hamann, F. W., Netzer, H., & Shields, J. C. 2000, ApJ, 536, 101
Heckman, T. M., Norman, C. A., Strickland, D. K., & Sembach, K. R. 2002, ApJ, 577, 691
Kaspi, S., Smith, P. S., Netzer, H., Maoz, D., Jannuzi, B. T., & Giveon, U. 2000, ApJ, 533, 631
Kaspi, S., et al. 2002, ApJ, 574, 643
Kellermann, K. I., Sramek, R., Schmidt, M., Shaffer, D. B., & Green, R. 1989, AJ, 98, 1195
Kimble, R. A., et al. 1998, Proc. SPIE, 3356, 188
Korista, K. T., et al. 1992, ApJ, 401, 529
Kriss, G. A. 2002, in ASP Conf. Ser. 255, Mass Outflow in Active Galactic Nuclei: New Perspectives, ed. D. M. Crenshaw, S. B. Kraemer, & I. M. George (San Francisco: ASP), 69
Krolik, J. H., & Kriss, G. A. 2001, ApJ, 561, 684
Laor, A., Fiore, F., Elvis, M., Wilkes, B. J., & McDowell, J. C. 1997, ApJ, 477, 93
Lehner, N., Savage, B. D., Wakker, B. P., Sembach, K. R., & Tripp, T. M. 2006, ApJS, 164, 1
Magorrian, J., et al. 1998, AJ, 115, 2285
Mathur, S., Elvis, M., & Wilkes, B. 1995, ApJ, 452, 230
McWilliam, A. 1997, ARA&A, 35, 503
Misawa, T., Yamada, T., Takada-Hidai, M., Wang, Y., Kashikawa, N., Iye, M., & Tanaka, I. 2003, AJ, 125, 1336
Monier, E. M., Mathur, S., Wilkes, B., & Elvis, M. 2001, ApJ, 559, 675
Moos, H. W., et al. 2000, ApJ, 538, L1
Morris, S. L., Weymann, R. J., Foltz, C. B., Turnshek, D. A., Shectman, S., Price, C., & Boroson, T. A. 1986, ApJ, 310, 40
Morton, D. C. 2003, ApJS, 149, 205
Murray, N., Chiang, J., Grossman, S. A., & Voit, G. M. 1995, ApJ, 451, 498
Narayanan, D., Hamann, F., Barlow, T., Burbidge, E. M., Cohen, R. D., Junkkarinen, V., & Lyons, R. 2004, ApJ, 601, 715
Netzer, H., et al. 2003, ApJ, 599, 933
Peterson, B. M., et al. 2004, ApJ, 613, 682
Petitjean, P., Riediger, R., & Rauch, M. 1996, A&A, 307, 417
Petitjean, P., & Srianand, R. 1999, A&A, 345, 73
Press, W. H., Teukolsky, S. A., Vetterling, W. T., & Flannery, B. P. 1992, Numerical Recipes in C: The Art of Scientific Computing (2nd ed.; Cambridge: Cambridge Univ. Press)
Proga, D., Stone, J. M., & Kallman, T. R. 2000, ApJ, 543, 686
Quijano, J. K., et al. 2003, STIS Intrument Handbook, Version 7.0 (Baltimore: STScI)
Reimers, D., Koehler, T., & Wisotzki, L. 1996, A&AS, 115, 235
Richards, G. T. 2001, ApJS, 133, 53
Richards, G. T., York, D. G., Yanny, B., Kollgaard, R. I., Laurent-Muehleisen, S. A., & vanden Berk, D. E. 1999, ApJ, 513, 576
Richter, P., Sembach, K. R., Wakker, B. P., Savage, B. D., Tripp, T. M., Murphy, E. M., Kalberla, P. M. W., & Jenkins, E. B. 2001, ApJ, 559, 318
Sahnow, D. J., et al. 2000, ApJ, 538, L7
Savage, B. D., Lehner, N., Wakker, B. P., Sembach, K. R., & Tripp, T. M. 2005, ApJ, 626, 776
Savage, B. D., & Sembach, K. R. 1991, ApJ, 379, 245
Schmidt, M. 1963, Nature, 197, 1040
Schmitt, H. R., Donley, J. L., Antonucci, R. R. J., Hutchings, J. B., Kinney, A. L., & Pringle, J. E. 2003, ApJ, 597, 768
Scott, J. E., Kriss, G. A., Brotherton, M., Green, R. F., Hutchings, J., Shull, J. M., & Zheng, W. 2004a, ApJ, 615, 135
Scott, J. E., et al. 2004b, ApJS, 152, 1
Sembach, K. R., Howk, J. C., Savage, B. D., & Shull, J. M. 2001, AJ, 121, 992
Sembach, K. R., & Savage, B. D. 1992, ApJS, 83, 147
Slavin, J. D., Shull, J. M., & Begelman, M. C. 1993, ApJ, 407, 83
Srianand, R., & Petitjean, P. 2000, A&A, 357, 414
Sutherland, R. S., & Dopita, M. A. 1993, ApJS, 88, 253
Telfer, R. C., Kriss, G. A., Zheng, W., Davidsen, A. F., & Green, R. F. 1998, ApJ, 509, 132
Telfer, R. C., Zheng, W., Kriss, G. A., & Davidsen, A. F. 2002, ApJ, 565, 773
Tremaine, S., et al. 2002, ApJ, 574, 740
Tripp, T. M., Giroux, M. L., Stocke, J. T., Tumlinson, J., & Oegerle, W. R. 2001, ApJ, 563, 724
Tripp, T. M., Lu, L., & Savage, B. D. 1996, ApJS, 102, 239
Tripp, T. M., et al. 2003, AJ, 125, 3122
Turnshek, D. A. 1988, in QSO Absorption Lines; Probing the Universe; Proc. QSO Absorption Line Meeting, ed. J. C. Blades, D. A. Turnshek, & C. A. Norman (Cambridge: Cambridge Univ. Press), 17
Verner, D. A., Barthel, P. D., & Tytler, D. 1994, A&AS, 108, 287
Vestergaard, M. 2003, ApJ, 599, 116
Voges, W., et al. 1999, A&A, 349, 389
Wakker, B. P. 2001, ApJS, 136, 463
———. 2004, Ap&SS, 289, 381
Wakker, B. P., et al. 2003, ApJS, 146, 1
Weymann, R. J., Morris, S. L., Foltz, C. B., & Hewett, P. C. 1991, ApJ, 373, 23
Weymann, R. J., Williams, R. E., Peterson, B. M., & Turnshek, D. A. 1979, ApJ, 234, 33
Wise, J. H., Eracleous, M., Charlton, J. C., & Ganguly, R. 2004, ApJ, 613, 129
Woodgate, B. E., et al. 1998, PASP, 110, 1183
Yuan, Q., Green, R. F., Brotherton, M., Tripp, T. M., Kaiser, M. E., & Kriss, G. A. 2002, ApJ, 575, 687